Angular-dependent interatomic potential for large-scale atomistic simulation of iron: Development and comprehensive comparison with existing interatomic models

Sergei Starikov ◉,[1,*] Daria Smirnova,[1,2] Tapaswani Pradhan ◉,[1] Yury Lysogorskiy,[1] Harry Chapman,[3]
Matous Mrovec ◉,[1] and Ralf Drautz ◉[1]

[1]*The Interdisciplinary Centre for Advanced Materials Simulation (ICAMS), Ruhr-Universität Bochum, 44801 Bochum, Germany*
[2]*Joint Institute for High Temperatures of RAS, 125412 Moscow, Russia*
[3]*Department of Materials, University of Oxford, Oxford OX1 3PH, United Kingdom*

The development of classical interatomic potential for iron is a quite demanding task with a long history background. A new interatomic potential for simulation of iron was created with a focus on description of crystal defects properties. In contrast with previous studies, here the potential development was based on force-matching method that requires only *ab initio* data as reference values. To verify our model, we studied various features of body-centered-cubic iron including the properties of point defects (vacancy and self-interstitial atom), the Peierls energy barrier for dislocations (screw and mix types), and the formation energies of planar defects (surfaces, grain boundaries, and stacking fault). The verification also implies thorough comparison of a potential with 11 other interatomic potentials reported in literature. This potential correctly reproduces the largest number of iron characteristics which ensures its advantage and wider applicability range compared to the other considered classical potentials. Here application of the model is illustrated by estimation of self-diffusion coefficients and the calculation of fcc lattice properties at high temperature.

I. INTRODUCTION

An accurate prediction of thermodynamic and mechanical properties of iron is of vital importance for materials engineering as Fe-based alloys are widely used as structural materials. Both thermodynamic and mechanical properties are to a great extent governed by crystal defects (from point defects to dislocations and planar defects). The scale of these objects and understanding of their fundamental properties, such as the formation, migration, and interaction energies, demands employment of atomistic modeling techniques such as molecular dynamics (MD). However, the description of interatomic forces in Fe is highly challenging and there exists a broad range of models with different levels of sophistication [1–5].

The diversity of the observed structural and magnetic phases of Fe stems from the complexity of atoms interactions, namely, the mixed metallic and covalent bonding due to overlapping *d* orbitals and the itinerant magnetism [6]. A subtle mixture of these two phenomena gives rise to a complex dependence of the potential energy and local magnetic order on the atomic environment. Even a precise description of elastic moduli is a quite challenging task demanding special approaches in first-principle calculations [3,4].

The peculiar character of Fe bonding is also reflected in the properties of its crystal defects. For instance, the most stable configuration of self-interstitial atom (SIA) in the body-centered-cubic (bcc) iron (α-Fe) is the $\langle 110 \rangle$ dumbbell (SIA-D110) [5,7,8]. This contrasts to other nonmagnetic bcc

metals, where SIA stabilizes in the $\langle 111 \rangle$ dumbbell (SIA-D111) orientation. Moreover, SIAs in iron tend to cluster together and form C15 phase inclusions, which is again atypical for other bcc metals [9–11]. Another outstanding property of iron is a strong dependence of vacancy formation and migration energies on temperature, which leads to a marked non-Arrhenius behavior of the self-diffusion coefficient [12–14]. A proper modeling of this phenomenon requires to take into account both the vibrational and magnetic degrees of freedom, for instance, by coupling molecular and spin dynamics (SD) [15–17]. It is important to note that such coupled simulations can be successful only when the atomistic and spin models describe accurately the atomic and spin interactions, respectively.

There exist a number of classical interatomic potentials for atomistic simulation of iron [1,18–29]. Mostly, they have been developed by fitting the potential functions to reproduce fundamental properties of Fe bulk phases (e.g., lattice parameters, elastic constants, or thermal expansion) and, in some cases, also properties of simple defects (e.g., formation energies of point defects, surfaces, or grain boundaries). However, these simplified models, which usually do not contain any explicit treatment of magnetism, suffer from a limited transferability and exhibit various deficiencies. Some of the well-known problems are an underestimation and incorrect shape of the Peierls energy barrier for the $\frac{1}{2}\langle 111 \rangle$ screw dislocation, underestimated surface energies, or spurious phase transformations [7,30].

Some of the deficiencies disappear when more sophisticated models are used. For instance, an improvement in dislocation properties was achieved by the magnetic

---

*sergei.starikov@icams.rub.de

bond-order potential [31–33], which is based on the tight-binding approximation and includes an explicit treatment of magnetism within the Stoner model. Recently, a new generation of machine-learning (ML) potentials have gained a lot of attention [34,35]. For Fe, there exist the Gaussian approximation potential (GAP) of Dragoni *et al.* [5] and a neural network (NN) potential of Mori *et al.* [36]. The ML models are based on fitting a large training database of total energies, forces, and stresses obtained from density functional theory (DFT) for a set of diverse reference atomic configurations. Hence, they are able to reproduce the formation energies of the targeted crystal defects with high accuracy [5]. However, the ML models also suffer from the low transferability outside of the training structures [36–38]. In addition, even though they are much faster than DFT approaches, ML potentials are inferior in speed by three to four orders of magnitude compared to the classical interatomic potentials [35,39,40]. Hence, large-scale MD simulations, such as studies of plastic deformation [41,42], crack propagation [30,43] under dynamic loading, nucleation and solidification from an undercooled melt [44–46], grains growth kinetics [47–49], or creation and evolution of defects at primary radiation damage [50–54] are impractical.

An attractive possibility to create both reliable and computationally efficient atomistic models is to carry out a ML development of the classical potentials [55,56]. In this way, the area of applicability can be substantially widened compared to that of potentials fitted in the conventional semiempirical way. At the same time, the relatively simple form of classical potentials is retained allowing simulations involving extensive timescales (up to 100 ns) and large atomic configurations (up to tens of millions of atoms). Already in 1994, Ercolessi and Adams [57] proposed to develop embedded atom method (EAM) potentials [58] by a force-matching procedure using a fitting database containing mostly DFT data. The key idea was to adjust the potential parameters to optimally reproduce not only total energies, but also atomic forces (and stresses) for a fine-tuned set of reference structures. In the recent years, this approach resulted in accurate and efficient classical potentials for different atomic systems such as U-Mo [59], U-N [60], Ti-Nb [61], Mg-H [62], and W-Re [63].

The aim of this work is twofold. First, we perform a detailed assessment of existing interatomic potentials for Fe by taking into account both their predictive accuracy and computational speed. We focus in particular on the behavior of crystal defects that are often the most challenging. Second, we carry out development of an angular-dependent potential (ADP) for Fe based on the ML approach by using the force matching for a large training set of DFT energies and forces. The predictive power and computational efficiency of the ADP potential is demonstrated on large-scale MD simulations of phase transformations, self-diffusion, and coupled MD and spin dynamics.

II. EXISTING INTERATOMIC POTENTIALS

In this section, we give a brief description of potentials for Fe developed in the last decades and available publicly through the NIST database [64,65]. In Table I, we have listed

TABLE I. List of the interatomic potentials for iron supplemented by the internal notations given within the frame of current work.

Reference	Notation
Ackland *et al.* (1997) [18]	Ac97
Mendelev *et al.* (2003) [19] Fe-5 ver.	Men03
Zhou *et al.* (2004) [20]	Zh04
Chamati *et al.* (2006) [21]	Ch06
Malerba *et al.* (2010) [25]	Mar07
Olsson (2009) [24]	Ol09
Chiesa *et al.* (2011) [26]	Chi11
Proville *et al.* (2012) [27]	MCM11
Mrovec *et al.* (2011) [31]	BOP11
Asadi *et al.* (2015) [28]	MEAM15
Dragoni *et al.* (2018) [5]	GAP18

all models considered in our study, accompanied by the original reference and an acronym that is used throughout the paper. It should be noted that we considered only potentials from the NIST database for which LAMMPS [66] parameter files are available. There exist additional potentials, accessible, for instance, via the KIM framework [67], which were omitted here. The current section concentrates mostly on potential functional forms, fitting techniques, and application purposes. The detailed validation of the models will be presented in Sec. IV.

Chronologically, one can see how the potential development followed enhancement in the computational resources and techniques during the last decades. The first many-body potential was developed by Ackland *et al.* [18] in 1997 (Ac97) as part of a binary Fe-Cu model. It was based on the Finnis-Sinclair model [68] and fitted to reproduce the experimental lattice parameter, elastic constants, cohesive energy, and vacancy formation energy of bcc Fe. In later work, Mendelev *et al.* [19] extended the fitting database to generate several EAM parametrizations that give a better description of defects as well as the liquid phase of Fe. The potential parameters were found to depend sensitively whether first-principles or experimental fitting data for liquid Fe were used in the fitting. From the five different parametrizations presented in Ref. [19], we used the Fe-5 version that shows the best overall representation of Fe bulk properties and was fitted to reproduce the experimental pair-correlation function of the liquid phase. The melting temperature modeled with the Mendelev's potential (Men03) [19] is only about 5% lower than the experimental value, while the previous Ac97 potential [18] overestimates it significantly (by about 30%). The Mendelev's potentials were further refined by Marinica *et al.* [25] resulting in an updated version (Mar07). This updated model shows a better representation of the thermal expansion of bcc Fe, and improved surface and point defect formation energies refitted to amended DFT data.

The EAM scheme presents a basis for several other Fe potentials. Zhou *et al.* [20] constructed a set of EAM potentials for 16 different metals including Fe (Zh04). All these potentials use the same formalism which makes it possible to combine them to simulate multicomponent systems. For example, simulation of misfit dislocations in CoFe/NiFe

multilayers was carried out using these models. Similarly, Olsson [24] developed a set of EAM potentials, including that for Fe (Ol09). The constructed models were used for a detailed study of the formation and migration of point defects. The initial fitting was performed in a similar way as that for Ac97 and afterwards corrected to ensure the correct stability of self-interstitial configurations. The EAM potential MCM11 reported in Ref. [27] was developed specifically to reproduce properties of the screw dislocation in Fe. Even though the predicted Peierls barrier compares well with that of first-principles calculations, the MCM11 sacrifices other properties.

An important aspect of Fe phase diagram is the bcc-fcc-bcc phase transitions occurring at high temperatures. The work of Chamati *et al.* [21] focused on reproducing properties of these two phases. They developed EAM potential (Ch06) using a fitting database containing the energies of bcc, face-centered-cubic (fcc), simple cubic, and diamond phases as functions of volume. The Ch06 potential is able to reproduce the thermal expansion, phonon spectra, and surface properties of fcc and bcc phases, but gives a poor description of the point defects. A different approach, based on Tersoff's empirical bond-order potential [23], was also shown to reproduce the phase transformations in Fe, but it significantly underestimated the surface energies.

As Fe bonding is mediated by directional *d* orbitals, several potentials with angular dependence have been developed recently [28,29] based on the modified EAM (MEAM) model. The MEAM15 model reported by Asadi *et al.* [28] is aimed at high-temperature properties of Fe. Here the melting point, volume changes at melting, and characteristics of solid-liquid interface were of highest interest, so the potential parameters were tuned to match the experimental melting point. An updated version of that model [29] also adds the correct representation of high-temperature elastic constants. Unfortunately, this version predicts the A15 phase to be more stable than the bcc phase so we used the original MEAM15 potential in our comparison.

As mentioned above, the classical potentials cannot describe different magnetic Fe phases so they usually aim at an effective description of some, mostly the ground magnetic state. Chiesa *et al.* [26] have attempted to complement an EAM interatomic potential by an approximate magnetic contribution via a second term to the embedding function, resulting in embedding energy being a sum of nonmagnetic and ferromagnetic contributions. The potential was aimed at the description of radiation damage and fitted to experimental bulk properties together with the nonmagnetic *ab initio* point defect energies and the screw dislocation core structure. In our tests, we adopted the CS3-33 version of their parametrization, here noted as Chi11.

Along with the classical potentials, we considered two more sophisticated models in our study: The magnetic bond-order potential (BOP11) [31,69] and the GAP model (GAP18) [5]. Both these models are significantly more computationally demanding than the empirical potentials. However, they allow to simulate some properties with higher accuracy than classical potentials. In addition, BOP11 gives opportunity to take into account various magnetic phases of Fe.

III. DEVELOPMENT OF ADP POTENTIAL

A. Force-matching technique

In this section, we detail the fitting of the ADP interatomic model using force matching. The form of the potential functions follows Ref. [70]. The potential energy U is given as

$$U = \sum_{i>j} \varphi(r_{ij}) + \sum_i F(\overline{\rho}_i) + \frac{1}{2} \sum_{i,k} (\mu_i^k)^2$$
$$+ \frac{1}{2} \sum_{i,k,l} (\lambda_i^{kl})^2 - \frac{1}{6} \sum_i v_i^2, \quad (1)$$

where

$$\overline{\rho}_i = \sum_{j \neq i} \rho(r_{ij}), \qquad \mu_i^k = \sum_{j \neq i} u(r_{ij}) r_{ij}^k,$$
$$\lambda_i^{kl} = \sum_{j \neq i} w(r_{ij}) r_{ij}^k r_{ij}^l, \qquad v_i = \sum_k \lambda_i^{kk}. \quad (2)$$

The indices i and j enumerate atoms while k, l = 1, 2, 3 refer to the Cartesian components of vectors and tensors. The first term in Eq. (1) corresponds to pair interactions between the atoms via a pair potential φ. The summation is performed over all j neighbors of the ith atom within the cutoff distance r_{cut} (which we set to 6.2 Å). The second term F is the embedding energy that is a function of the total electron density $\overline{\rho}$. Hence, the first two terms in Eq. (1) correspond to the conventional EAM model [71]. The additional terms μ and λ introduce noncentral interactions through the dipole vectors and quadrupole tensors. These terms give the ADP model additional flexibility to describe angular interactions that become especially important in distorted bonding environments around crystal defects [72].

Each of the functions in Eqs. (2) is described by a set of cubic splines, whose parameters are optimized using force-matching algorithms realized in the POTFIT code [73,74]. The fitting procedure proceeds by minimization of the cost function Z, which includes two parts: (i) Z_f corresponding to atomic forces f, and (ii) Z_A corresponding to an integral quantity A (in our case, A is either the energy or one of the six components of the stress tensor of the reference configuration), such as

$$Z = Z_f + Z_A, \quad (3)$$

$$Z_f = \sum_{i=1}^{N_f} \sum_{\alpha = x,y,z} W_C (f_{i\alpha}^{ADP} - f_{i\alpha}^{DFT})^2, \quad (4)$$

$$Z_A = \sum_{j=1}^{7N_C} W_C W_A (A_j^{ADP} - A_j^{DFT})^2. \quad (5)$$

N_f is the number of atoms for which the values of forces f are taken into account during the minimization. N_C is the number of reference configurations with weights W_C. For a single configuration, we have one value of the energy and six components of the stress tensor. Moreover, general weights W_A are included to allow an independent optimization of the function Z_A for all energies and stress components. We chose $W_A = 2000$.

TABLE II. Description of the reference configurations. Here N_c is the number of structures of the given type included in the fitting database. n_{at} is the number of atoms in a given structure, W_C is the attributed individual weight. For convenience, configurations with the same structure are grouped and the minimum and maximum values of the effective temperature T (in K) and atomic volume V (in Å^3 per atom) are specified.

Structure	N_c	n_{at}	W_C	T_{min}–T_{max}	V_{min}–V_{max}
Configurations with attributed forces					
bcc	3	128	1	600–700	10.5–11.5
bcc	6	250	2	300–1800	9.5–13
dis-bcc	8	~360	2	300–600	9.7–14
def-bcc	4	250	10	300	10.8–12.2
fcc	1	256	2	1600	11.1
liquid	1	249	2	2300	11.2
(210)GB	1	240	2	350	10.8
(332)GB	1	176	2	350	10.9
Configurations without attributed forces					
bcc	1	250	100	0	11.5
bcc	1	250	100	0	10.5
vacancy	1	249	100	0	11.5
di-vacancy	1	248	100	0	11.5
SIA-D110	1	251	200	0	11.5
SIA-D111	1	251	200	0	11.5
di-SIA	1	252	200	0	11.5
fcc	1	108	50	0	14.0
fcc	1	108	10	0	11.5
fcc	1	108	10	0	10.1
hcp	1	192	10	0	8.5
(111)GB	1	144	25	0	11.5
(112)GB	1	192	25	0	11.5
(320)GB	1	192	25	0	11.5
(510)GB	1	312	25	0	11.5

B. Description of the reference structures

Information about atomic configurations used for the ADP fitting is given in Table II. Each of the reference structures contained about 100–360 atoms in a simulation box with periodic boundary conditions (PBC). All configurations were obtained from classical atomistic simulations (MD or static) using the Chi11 potential, carried out at different temperatures T and volumes V. Hence, averaged displacements of atoms from their equilibrium lattice sites correlate with the given T. All classical calculations were performed using the LAMMPS molecular dynamics simulator [66].

The configurations listed in Table II are divided into two groups. The first group of structures contains the fragments of classical MD trajectories and aims at the DFT calculations of forces, energies, and stresses. These configurations correspond to various Fe phases (bcc, fcc, and liquid) at different T and V. The "dis-bcc" configurations represent largest supercells containing screw dislocations (one or two) and open surface. In addition, this group includes also configurations of several tilt grain boundaries (GB). Most configurations were fitted with the weight W_C equal to 1 or 2. The only exception was made for the uniaxially deformed bcc lattices "def-bcc" which were attributed higher weights $W_C = 10$ to achieve accurate elastic properties. The broad ranges of T and

V used for sampling these configurations provide an extensive representation of distinct atomic arrangements in the fitting database.

The structures in the second group were used for an energy minimization with DFT approach. Therefore, only the energies of these structures were used in the fitting. These configurations included perfect fcc, hexagonal-closed-packed (hcp), and bcc bulk phases, different tilt GBs, and point defects. Individual weights W_C chosen for these structures are also listed in Table II.

In total, 41 configurations were used for the potential construction. Apart from the 40 structures listed in Table II, we used a configuration representing Fe at low density. Such structure is necessary to ensure that the potential energy goes to zero for large interatomic distances. In total, the reference data set included 41 energy values, 150 stress tensor values (6 stress components per configuration with forces), and 20 040 values of the force components.

The reference DFT calculations were done using the Vienna *ab initio* simulation package (VASP) [75]. The Brillouin zone was sampled using a $2 \times 2 \times 2$ Monkhorst-Pack **k**-point mesh. The cutoff energy of the plane-wave basis set was equal to 430 eV. We used the projector augmented wave (PAW) pseudopotential included in the VASP package (version 5.4.1) and the exchange-correlation functional within generalized-gradient approximation (GGA) in the form of Perdew-Burke-Ernzerhof [76]. The achieved electronic convergence of total energy in each calculation was lower than 0.001 eV (or 10^{-5} eV/atom).

For each configuration, we carried out both nonmagnetic and magnetic (spin-polarized) calculations. The initial magnetic ordering for most configurations in the spin-polarized calculations was the ferromagnetic (FM) state. Only the fcc and hcp phases were initially given with the antiferromagnetic (AFM) single-layer magnetic ordering since the FM phases have higher energies. For some defect configurations, the DFT calculations predict local magnetic moments on some atoms to deviate strongly from the bulk FM values. Hence, for each reference configuration the ground magnetic (GM) state corresponding to the minimal potential energy was used at the fitting. It should also be noted that the nonmagnetic calculations were used later to fit an additional ADP parametrization (see below).

C. ADP parametrization

Figure 1 shows all fitted ADP functions. Each function is described by cubic spline and the total number of the fitted parameters (i.e., total number of splines nodes for all functions) is 73. The estimated accuracy of the fitted model with respect to the reference DFT data is about 105 meV/Å for the forces, 14 meV for the energies, and 0.22 GPa for the stresses. The energy and force comparisons are shown in Fig. 2. This accuracy is close to the limit that can be achieved with a classical potential of ADP (or EAM) type [35,72]. The final potential parametrization in the LAMMPS *setfl* format can be downloaded from the NIST interatomic potential repository [64,65]. Also, the Supplemental Material [77] contains the cubic spline parameters of the developed potential.
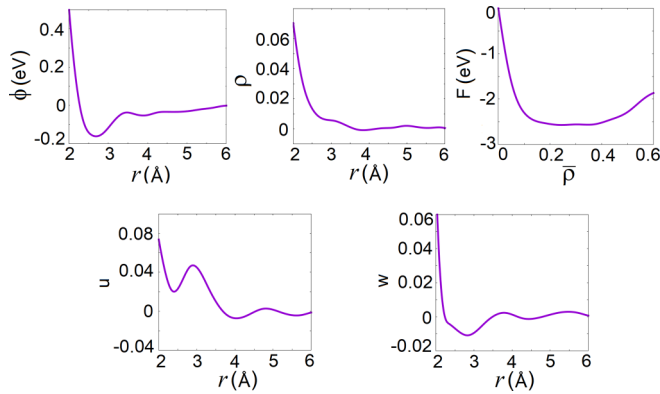
FIG. 1. Fitted functions of the developed ADP potential.

As this ADP parametrization is fitted to spin-polarized DFT results, it is aimed at reproduction of the GM state energies. Owing to this fact, this ADP model can provide a trustworthy description of Fe only at moderate temperatures up to about 600 K where magnetic excitations are not so important. A similar application range was stated for the Chi11 potential of Chiesa *et al.* [26]. At higher temperatures, the results of atomistic simulations should be analyzed with caution. An improved description of high-temperature behavior may be obtained by combination of MD and SD simulations [15–17]. However, as will be shown later, the ADP model is able to predict qualitatively correct results for properties of disordered structures (e.g., liquid phase or some grain boundaries) even when no SD is employed. This is probably related to the fact that the temperature-induced magnetic excitations do not play significant role in behavior of poorly ordered structures [78,79] where magnetic disorder takes place even in GM state at low temperature.

As an additional task, we developed another ADP parametrization fitted to nonmagnetic (NM) DFT results that may be combined with advanced SD simulation [16] to study the properties at temperatures close to or higher than the Curie temperature. The NM model is described in more detail in Appendix A.

IV. COMPARISON OF POTENTIALS

This section provides an extensive validation of all considered potentials together with our ADP potential. Here, we mostly analyze the properties that can be also computed using
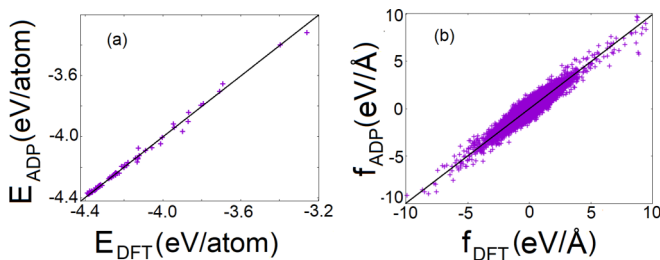

FIG. 2. Comparison of ADP prediction with respect to the reference DFT data: (a) energy per atom averaged over all atoms in the configuration; (b) force per atom.

DFT to obtain an unbiased comparison. The aim of this critical assessment is to delimit clearly the applicability range for all potentials.

A. Fundamental properties of the bcc Fe phase

Table III presents a comparison of the fundamental properties for the bcc ground state predicted by all potentials together with DFT and experimental results. It can be seen that all potentials agree very well with the DFT and/or experimental data since the basic properties such as the lattice parameter, elastic constants, and the cohesive energy were used in the fitting. Surprisingly, the GAP model shows the most pronounced disagreement with the experimental data for the cohesive energy. This discrepancy is due to nonphysical behavior of the model at low densities (the energy-volume curves for the whole interatomic range are shown in Appendix B).

Table III also contains approximate values of normalized MD computational time t_c illustrating relative computational costs of the potentials. We estimated t_c using a benchmark MD simulation of 3456 atoms at room temperature for 1000 steps (on a single CPU). The LAMMPS molecular dynamics simulator [66] was used for all potentials except for BOP11 which was carried out using the BOPFOX code [85]. The analysis of the computational efficiency indicates that BOP and GAP are significantly slower than the other potentials while the ADP model is only in three to four times slower than the most efficient EAM potentials. Such result ensures applicability of the ADP for large-scale MD simulations, as will be shown below.

B. Energy-volume curves

A correct representation of the relative phase stability is one of the fundamental requirements for any interatomic potential. For this purpose, we evaluated the energy E versus volume V curves for four important lattice types: bcc, fcc, A15, and C15. Figure 3 shows the E-V dependencies for all potentials and DFT taken from Refs. [10,86].

According to DFT, the FM state is the most stable magnetic ordering for bcc, A15, and C15 phases. However, for the fcc lattice, the most stable magnetic state changes with decreasing volume from the FM state to the antiferromagnetic double-layer (AFMD) state and further to the AFM state. In contrast to models based on the electronic structure [2,12,31], classical interatomic potentials are not able to differentiate between the magnetic phases. Among the tested models, only BOP11 can take into account various magnetic orderings. Nonetheless, two features on the DFT E-V dependencies shown in Fig. 3 deserve additional discussion: (1) an intersection of the bcc and fcc curves at compression, and (2) the absence of an intersection of the bcc curve with any other curves at expansion (at least for $12 < V < 14$ Å^3). A correct reproduction of these features is significant for a reliable description of Fe phase transformations. Specifically, the fact that the fcc phase becomes more stable than the bcc phase under compression is a necessary condition for the existence of thermodynamically stable fcc phase in the Fe phase diagram (see Ref. [86]). This feature is correctly reproduced only by BOP11, Ch06, and

TABLE III. Basic properties of bcc Fe described by the investigated interatomic potentials. The listed properties include lattice parameter at zero temperature a_0 in Å, cohesive energy E_{coh} in eV/atom, elastic constants C_{ij} in GPa, and linear thermal expansion α_L (in temperature range from 300 to 600 K) in 10^{-5} K^{-1}. The last column contains normalized values (by 7.9×10^{-7} s/step/atom) of a computational time t_c from an MD simulation.

	a_0	E_{coh}	C_{11}	C_{12}	C_{44}	α_L	t_c
Expt.	2.855[a]	4.28	240[b]	136[c]	121[c]	1.35[d]	
DFT	2.834[e]		297[e]	151[e]	105[e]		
Ac97	2.867	4.316	243	145	116	0.94	1.0
Men03	2.855	4.134	244	145	116	0.91	4.7
Zh04	2.866	4.291	230	136	117	1.17	2.9
Ch06	2.867	4.280	241	147	114	1.32	3.1
Mar07	2.855	4.122	243	145	116	1.05	7.0
Ol09	2.870	4.279	240	136	121	1.29	2.1
Chi11	2.867	5.79	244	138	122	0.8	2.6
MCM11	2.815	4.123	243	145	116	1.61	4.7
BOP11	2.850	4.399	265	164	123	—	2979
MEAM15	2.851	4.292	231	135	116	1.13	10.5
GAP18	2.835	0.14	286	154	104	1.29	54430
ADP	2.830	4.376	255	116	113	1.37	11.4

[a]Reference [80].
[b]Reference [81].
[c]Reference [82].
[d] Reference [83].
[e]Reference [84].

ADP potentials. On the other hand, many potentials including Ac97, Men03, Mar07, Ol09, MCM11, and GAP18 incorrectly predict a phase transformation when the bcc crystal is expanded. It has been shown recently [30] that this deficiency leads to various artifacts during fracture simulations. Hence, our validation shows that only BOP11 and ADP reproduce the features of E-V curves correctly while all other models exhibit various deficiencies and their overall description of the structural hierarchy over the considered density range is rather poor. Complete E-V curves over a broader range of volumes up to the potential cutoff are shown in Appendix B.

In the analysis of structural stability, we did not include results for the hcp phase as the calculated energy difference between the hcp and fcc phases is less than 0.04 eV at all considered volumes. These results can be found for all tested potentials in the NIST database [64,65]. In general, most of the tested models are unable to predict the phase transition from bcc to hcp under compression, which is observed experimentally [87–89]. The only exception is the Ch06 model, which partially reproduces the stabilization of hcp phase in a narrow pressure region (see Ref. [90] for more detailed description of the calculated phase diagram).

C. Phonons

Vibrational properties are essential for analysis of the material behavior at finite temperatures. We computed the phonon density of states (DOS) for bcc Fe using the small displacement method as implemented in the PHONOPY software package [91]. All obtained phonon DOS profiles are shown in Fig. 4. Most potentials demonstrate a good agreement with the experimental data [92]. Only the MCM11 and MEAM15 potentials exhibit significant inconsistencies with the measured phonon DOS.

D. Formation and migration energies of point defects

One of the general tests for any interatomic potential is the representation of vacancy formation energy E_{vac}^f. We evaluated the vacancy formation energy for all models using a periodic supercell with dimensions of $5a_0 \times 5a_0 \times 5a_0$. For validation, we compared the results with those of three DFT studies taken from Refs. [5,7,93]. The comparison shown in Fig. 5 reveals that most potentials underestimate E_{vac}^f with GAP, ADP, and Mar07 giving the best agreement with DFT.

For Fe self-interstitials, there exist five important configurations that are (in order of decreasing stability) SIA-D110, tetrahedral SIA, SIA-D111, SIA-D100, and octahedral SIA. A proper description of SIA thermodynamics and kinetics requires that not only the ground-state configuration and its energy is reproduced correctly, but also the hierarchy of the other SIA configurations is captured well, namely, $E_{110}^f < E_{Tet}^f < E_{111}^f < E_{100}^f < E_{Oct}^f$. In Fig. 5, we compare the calculated formation energies of SIAs with the existing DFT data [5,7]. It is clear that to capture the subtle energetic of various SIA configurations is very challenging and only the GAP18 model, which was, however, fitted using a large data set of defect configurations including SIA, is able to provide a reliable description of SIA defects in comparison with DFT. All other potentials exhibit discrepancies ranging from several tenths to more than one eV. In addition, only two classical potentials (ADP and Mar07) predict the right energy hierarchy of SIA defects.

For the monovacancy, we evaluated also its migration energy at zero pressure and temperature. For this purpose, we used the nudged elastic band (NEB) method [94]. The migration path along the $\langle 111 \rangle$ direction was sampled using 27 images. Due to the large number of models considered, the results are shown in three panels of Fig. 6. A first noticeable
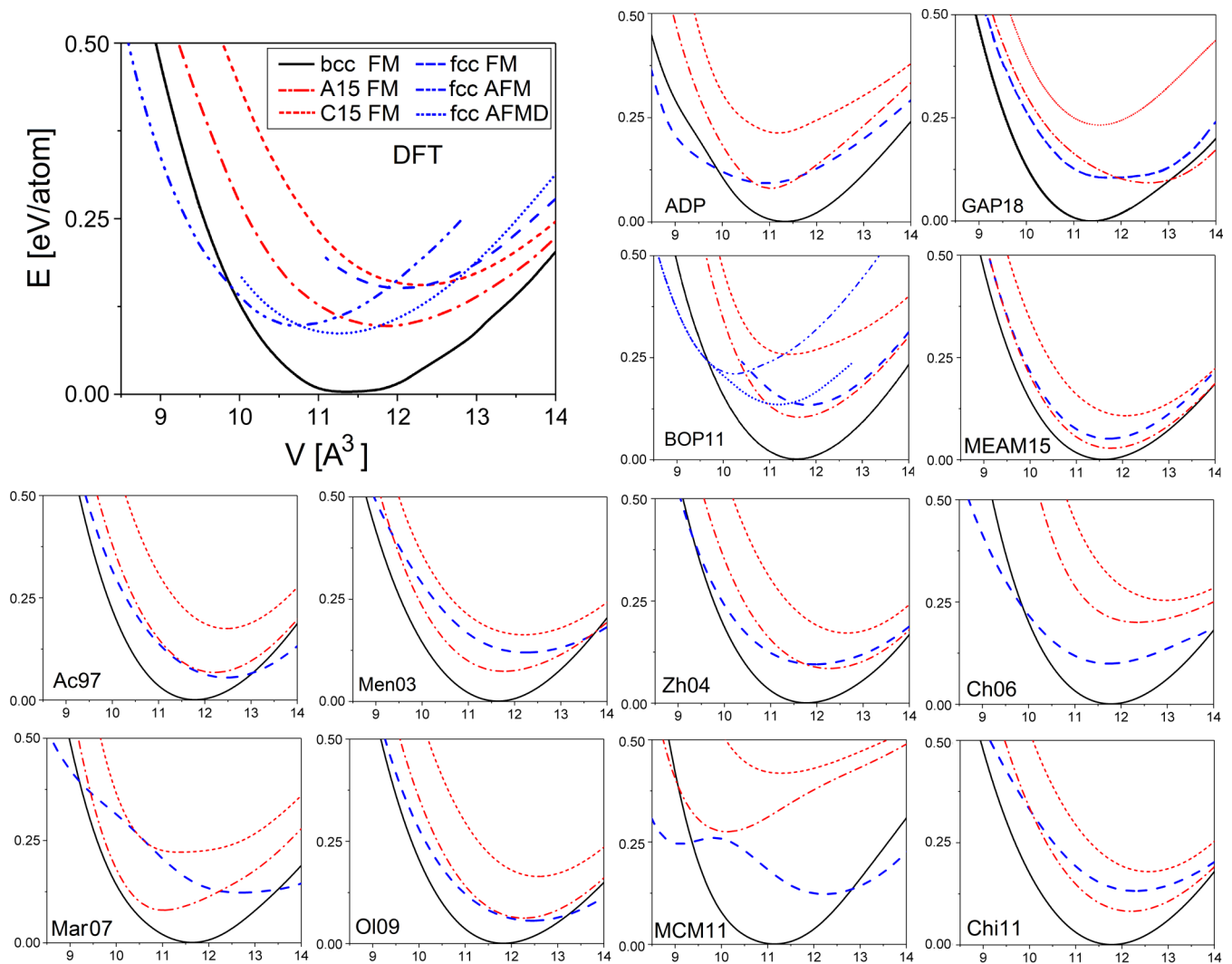
FIG. 3. Energy-volume curves for the bcc, fcc, A15, and C15 phases of iron. DFT data are taken from Refs. [10,86].

feature is a double-hump migration profile with a metastable transition state predicted by many potentials. Such peculiarity is not seen in the DFT calculations, which do not predict any local minimum corresponding to the transition state. Our DFT migration barrier of 0.7 eV is consistent with other reported values [93,95,96]. The best agreement with DFT data was obtained for Zh04, Ol09, and GAP18 potentials. In general, the vacancy migration energy E_{vac}^m, corresponding to the maximum height of the barrier, lies within 0.6–0.8 eV for most potentials. The exceptions are the Ch06 and MEAM15 potentials with significantly underestimated values and BOP11 which gives a much higher value of more than 1.0 eV.

We also estimated the sum of the energies describing formation and migration of a vacancy: $E_{vac}^f + E_{vac}^m$. With the ADP its value is close to the experimentally obtained self-diffusion activation energy ($\approx$2.9 eV) for the FM bcc phase [97,98]. Generally, the same agreement is seen between the experiment and $E_{vac}^f + E_{vac}^m$ obtained from DFT calculations. Summarizing characteristics of a vacancy given by ADP, we can conclude that the accurate representation of the involved energies can ensure adequate simulation of the vacancy diffusion

in FM bcc Fe. A more detailed description of diffusion-related phenomena is given in Sec. V.

E. Binding energies of point defects

Interactions between point defects are crucial for simulations of collision cascades and microstructural evolution during radiation damage. For example, a pair of SIA defects attract each other, eventually forming a nonparallel (NPC) di-interstitial configuration with triangular symmetry [25,99,100]. Such defect configuration may be considered as a component of C15 inclusion. We calculated the binding energy for this defect (E_{NPC}^b) as shown in Fig. 7. For most potentials, the computed E_{NPC}^b is close to the DFT value [5]. However, only three potentials (MCM11, GAP18, and ADP) yield the NPC configuration as the most stable one. For the remaining nine potentials, the di-SIA ground state corresponds instead to a $\langle 110 \rangle$ linear arrangement. Since MCM11 predicts a wrong energy hierarchy of SIA configurations, ADP and GAP18 are the most preferred models for atomistic simulation of SIAs clusterization and formation of the C15 inclusions [10,101].
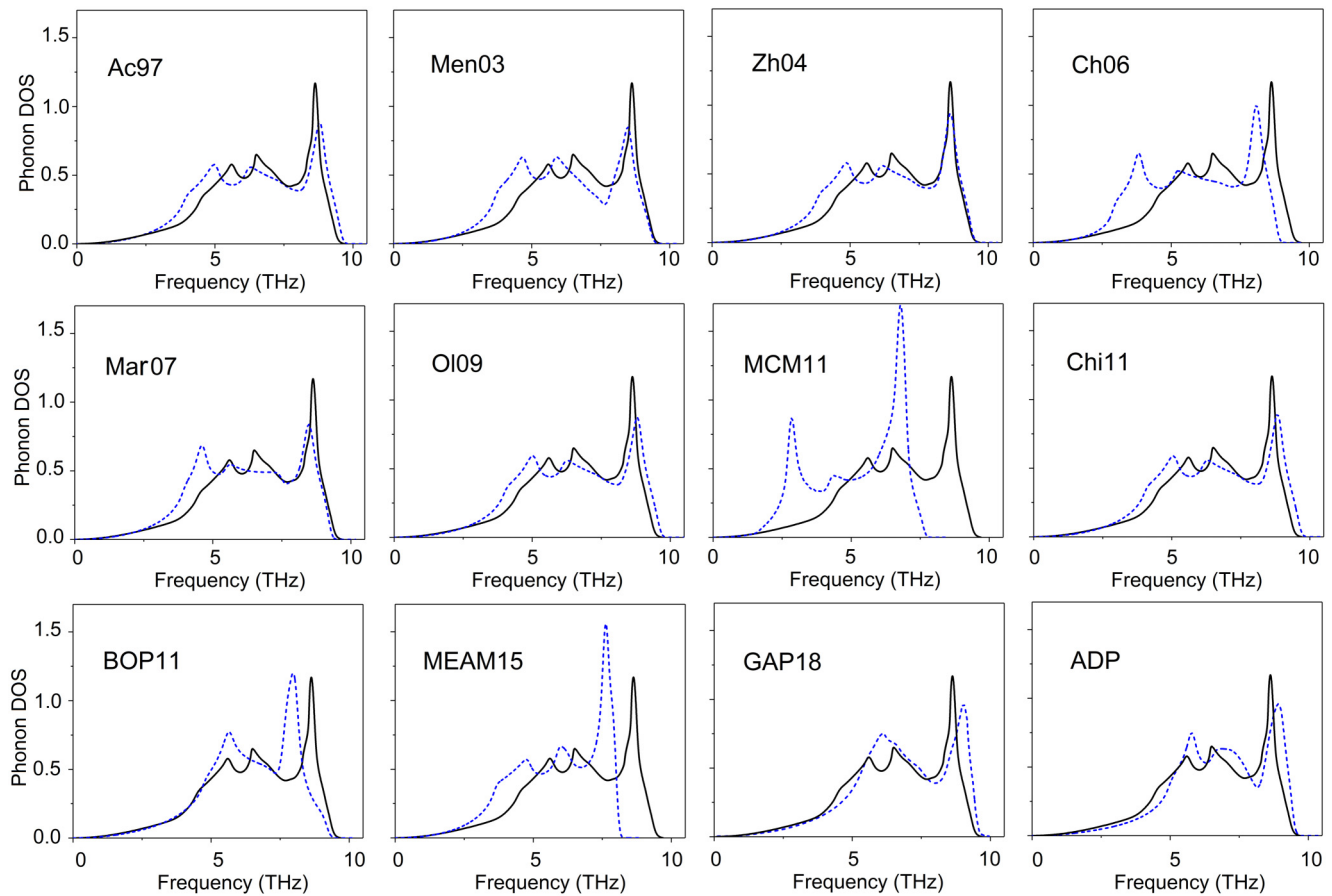
FIG. 4. Phonon DOS for bcc Fe calculated with various interatomic potentials. The experimental data [92] are shown by the black solid line.

We also paid attention to the nature of vacancy binding. According to the previous research, the binding energy for two vacancies in bcc Fe is relatively small, about 0.2 eV for the nearest-neighbor (1NN) orientation and about 0.25 eV for the second-nearest-neighbor (2NN) position [5,102]. We did not limit our validation to these two configurations but investigated the divacancy interactions up to the fourth-nearest neighbor (4NN). The calculated energies are plotted in Fig. 8 together with DFT results from Ref. [5]. Most tested potentials reproduce the binding energies with acceptable accuracy, and only Ol09 and MEAM15 show a significant disagreement with DFT.

F. Grain boundaries and surfaces

In this section, we move from the point defects to more challenging configurations including surfaces and grain boundaries. First, we focus on four symmetric tilt GBs, namely, $\Sigma3(112)$, $\Sigma5(310)$, $\Sigma5(210)$, and $\Sigma13(510)$. The GB structures were optimized by relaxing atomic positions, cell dimensions, as well as lateral translations of the two grains. A detailed description of the investigated GBs is given in our recent work [103]. The calculated GB energies for all potentials together with reference DFT values [104] are displayed in Fig. 9. The results show that most classical potentials strongly underestimate the GB energies as was found

also in other studies [30,105]. The best agreement with DFT data is seen for the Chi11, ADP, BOP11, and GAP18.

In addition to GBs, we also investigated several low-index surfaces which play an important role in simulations of fracture [30] or crystal growth. In diffusion studies, open surfaces allow to achieve the equilibrium concentration of point defects inside the bulk [103,106–109]. We calculated the surface energy E_{sur} using supercells with PBC along the lateral directions and 10 Å of vacuum region normal to the surface. Four different surface orientations were studied: (100), (110), (211), and (111). Figure 10 summarizes the energies obtained for all tested potentials. Ch06, ADP, MEAM15, and GAP18 reproduce the absolute surface energies with the highest accuracy in comparison with DFT [5]. However, we observed that in MD simulations using GAP18 most of the surfaces become unstable at finite temperature. Due to the small cohesive energy and unphysical E-V curves at large volumes (see Appendix B), surface atoms tend to spontaneously detach at surface steps or curved surfaces, leading to a spontaneous vaporization. The GAP18 potential is therefore not suitable for any simulations involving surfaces at elevated temperatures.

G. Dislocations and stacking faults

Classical atomistic simulations have been used extensively in studies of dislocations to gain insights into microscopic
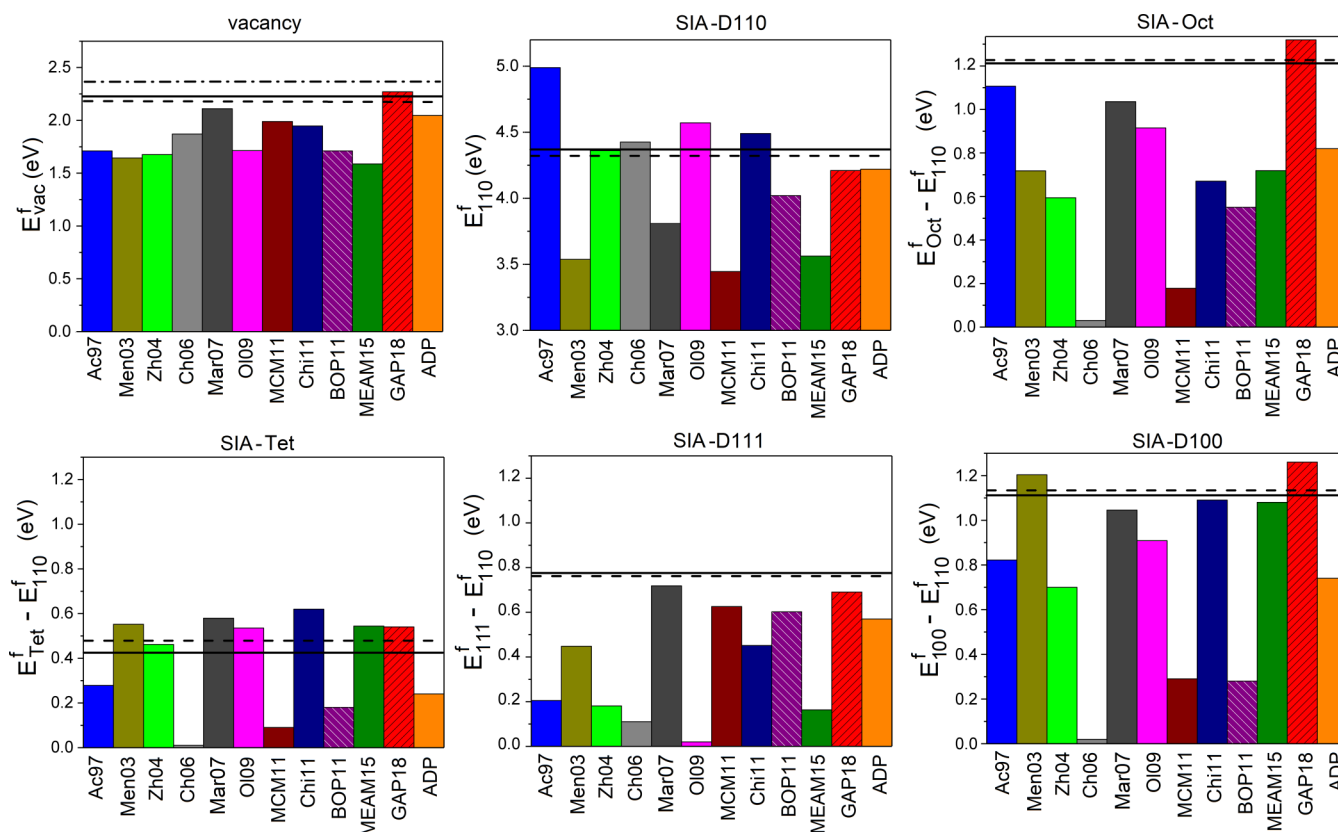
FIG. 5. Formation energy of point defects in bcc Fe at zero pressure and temperature. Each bar shows the value calculated with one of the potentials. Formation energies of SIA in nonground states are shown relative to the energy of 110 dumbbell. Black horizontal lines correspond to DFT calculations reported in various works: Solid line, Ref. [5]; dashed line, Ref. [7]; dashed-dotted line, Ref. [93].

origins of the plasticity of bcc metals [41,42,110–112]. In this work, we considered two types of dislocations, the screw (S111) and the mixed (M111) dislocation, both with the Burgers vector $b = \frac{1}{2}\langle 111 \rangle$. The S111 dislocation has a compact, nonplanar core and governs the low-temperature plastic deformation while the M111 dislocation is planar and expected to possess a low Peierls stress.

For S111, DFT calculations [5,10,113–115] predict the so-called nondegenerate ground-state structure, also known as the "easy" core. We investigated the S111 core structures for all tested potentials and compared them using the usual differential displacement (DD) plots. All potentials, which

correctly reproduced the nondegenerate core structure (except of the Ac97, Ol09, and MEAM15 models), were further tested for additional dislocation properties.

The most important property related to dislocation mobility is the Peierls barrier [116]. We evaluated the Peierls barrier under zero stress using the the NEB method. The obtained barrier profiles are shown in Fig. 11 together with the reference DFT values. Most potentials exhibit marked quantitative or even qualitative deficiencies, with their Peierls barriers having a "double-hump" shape with a local minimum corresponding to an intermediate state, which contrasts with the DFT result [26,31,117]. The intermediate minimum usually corresponds
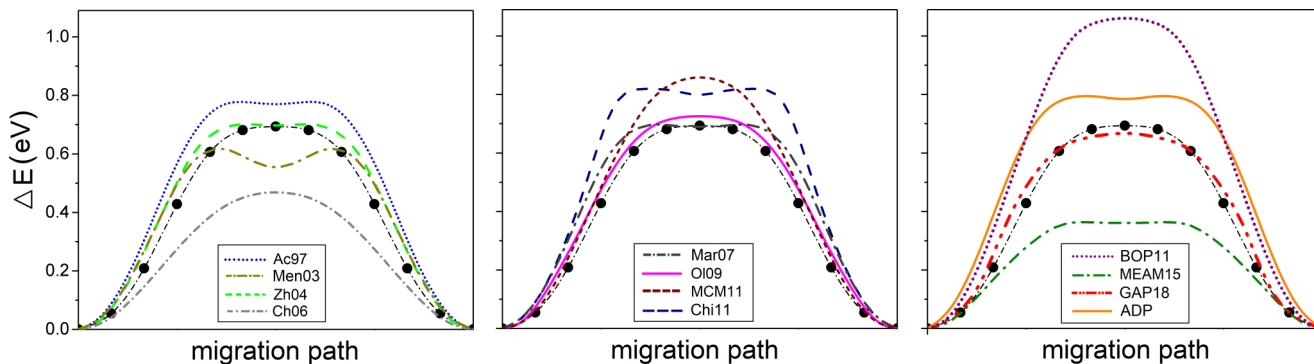

FIG. 6. Vacancy migration barrier calculated using NEB for different interatomic potentials; full black circles show DFT result from this work.
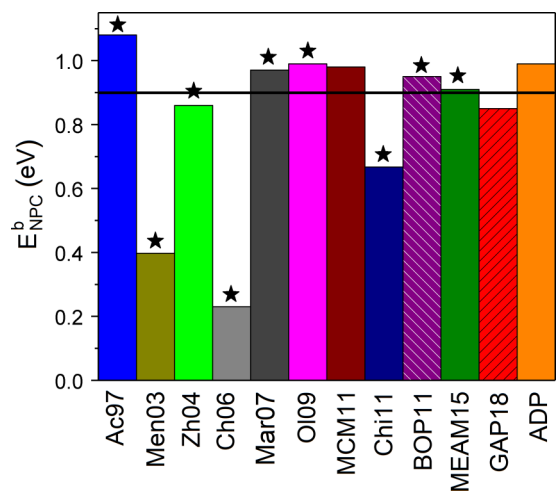
FIG. 7. Binding energy of di-SIA in the NPC configuration. Solid horizontal line shows the energy calculated with DFT in Ref. [5]. Stars indicate potentials predicting ⟨110⟩ di-SIA ground state.

to a spurious split core configuration that may alter the preferred dislocation glide system. These deficiencies have been extensively analyzed [115,117,118] and are most likely related to the simplified functional forms of the potentials and the lack of a proper description of the unsaturated directional
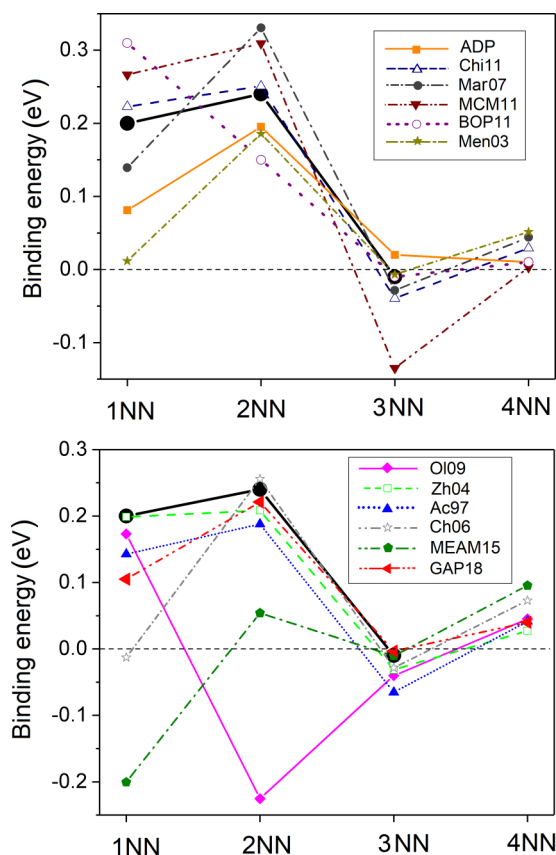

FIG. 8. Binding energy of divacancy in bcc Fe as function of the separation. Full black circles correspond to the DFT results from Ref. [5].

bonds. Marinica *et al.* [27] were able to specifically fit the correct shape and the height of the barrier but only by significantly sacrificing the overall transferability of the potential. The correct description of dislocation properties, especially its response and variations under applied stress, therefore present an extremely stringent test for classical interatomic potentials. Aside from the MCM11 potential, the only model that reproduces well both the shape and the height of the Peierls barrier is the more sophisticated BOP11 model.

For M111, there exist two core variants with distinct symmetries and different locations of dislocation center along the [112] direction on the {110} glide plane [119]. One of the cores is centered on the atoms (labeled as AC core), the other core is centered on the bonds between the atoms (labeled as BC core). Recent DFT calculations [119] revealed that in transition bcc metals the AC core corresponds to the minimum energy configuration while the BC core corresponds to the transition state (energy maximum). However, in Fe the energy difference is extremely small (about 1 meV/b) and both cores are energetically almost degenerate with a very flat Peierls barrier. Similarly to S111, most potentials have difficulty to reproduce the M111 energetics (see Fig. 11). Most correct descriptions of the Peierls barrier are provided by BOP11 while Ch06, Mar07, and GAP18 give small barrier heights but a reversed stability of both cores. ADP predicts the right shape of the Peierls barrier, but the height is slightly overestimated.

In relation to dislocation properties, we paid attention to relevant stacking faults (SF). The properties of stacking faults are related not only to dislocation core structures, but also to twinning processes and fracture. Based on the concept of generalized stacking fault energy (GSFE) surface [120] (also known as γ surface), we evaluated variations of the cross sections of relaxed (110) γ surfaces along [1$\bar{1}$0] and [1$\bar{1}$1] directions for the tested potentials. Similar dependencies for some potentials have been reported previously in Refs. [30,121]. As in Ref. [121], we examined how the profiles change with strain, namely, 5% equibiaxial strain in the [110] and [1$\bar{1}$0] directions. The computational results for ADP, Chi11, GAP18, and MCM11 are shown in Fig. 12. Results obtained for Ch06, BOP11 (see Ref. [121]), GAP18, and ADP potentials show the best agreement with DFT for both unstrained and strained cases. In contrast, Men03, Zh04, Mar07, Chi11, and MCM11 potentials show a propensity for phase transformation to a close-packed structure under applied stress that lead to unphysical fracture behavior [121]. Moreover, Mar07 and MCM11 models revealed the structure transformation even for the strain crystal without shift.

H. Strengths and limitations of the ADP potential in comparison with other models

Based on the extensive validation presented above, we can assess general accuracy of the tested interatomic potentials. The stability of different crystal structures is the first key benchmark providing an estimation of the model accuracy. The comparison of E-V plots in Fig. 3 shows that BOP11 and ADP models provide the most accurate representation of the energy hierarchy for the considered structures. It is worth mentioning that none of the tested models included the A15 and C15 phases in the potential fitting. Hence, the E-V curves
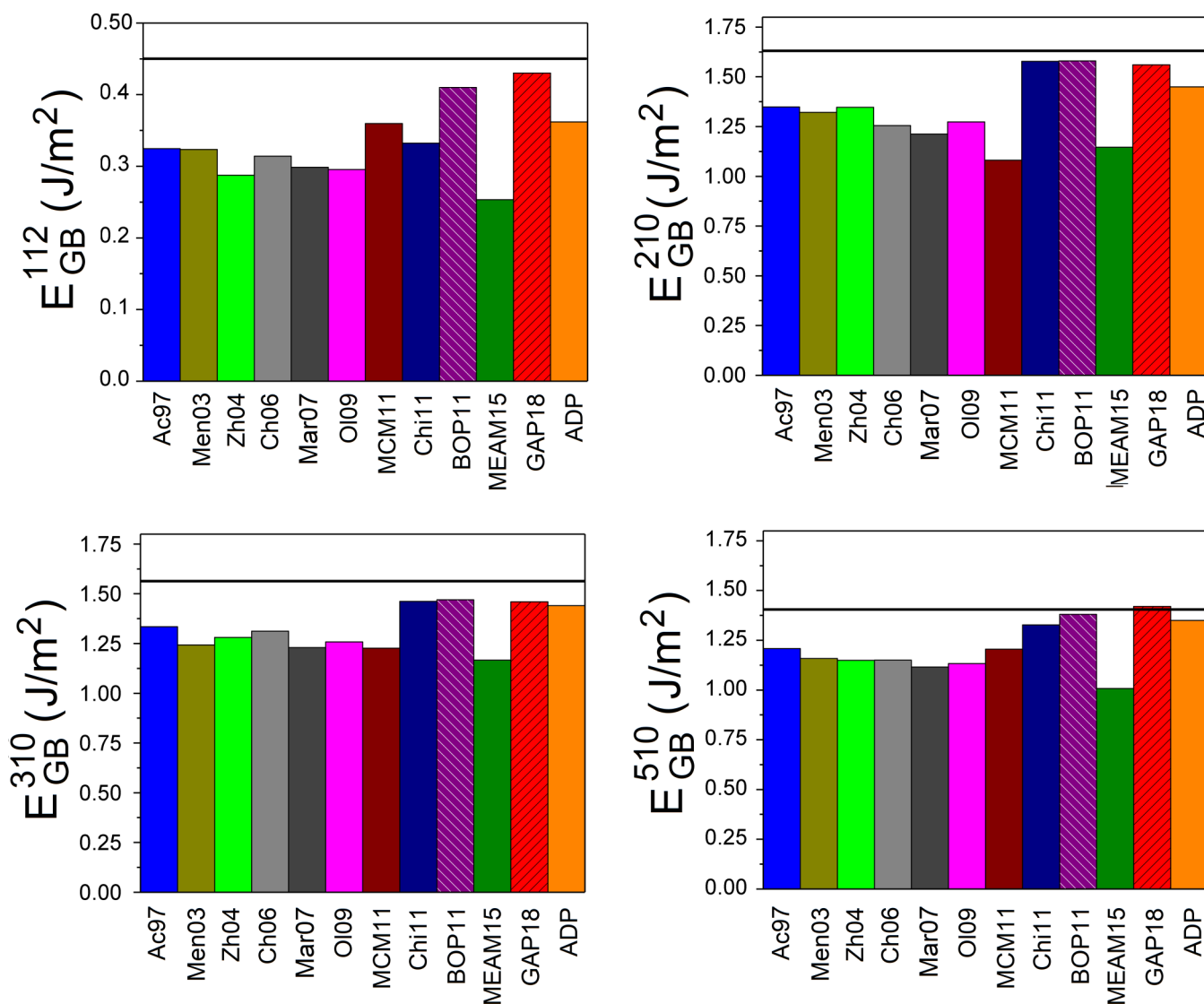
FIG. 9. Energies of different symmetric tilt grain boundaries. Horizontal solid lines show results of DFT calculations from Ref. [104].
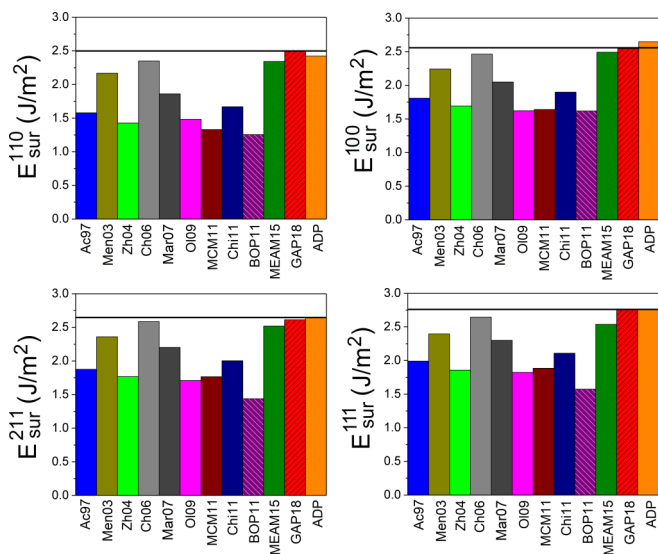

FIG. 10. Surface energies calculated for the different surface orientations. Black horizontal lines show DFT results from Ref. [5].

for these two structures can be considered as one indicator of transferability of the tested potentials. For instance, the inability of GAP18 to reproduce correctly the structural hierarchy is clearly due to absence of these structures in the training set used for the model development. In principle, this shortcoming can be fixed by adding new reference data, but it is necessary to pinpoint all essential configurations in advance.

One of the most valuable characteristics of our ADP model is a reliable description of point and planar defects. In this respect, the model stands out in accuracy among the tested potentials, second only to the GAP18 model. For instance, only the GAP18 and ADP potentials reproduce quantitatively correctly both GB and surface energies, while the other models describe either one or the other. The predicted formation, migration and binding energies for the point defects calculated with GAP18 and ADP models deviate from the DFT reference values by less than 0.2 eV.

The most pronounced limitation of our ADP model is the wrong shape and the underestimated height of the Peierls energy barrier for the S111 dislocation. However, this feature is
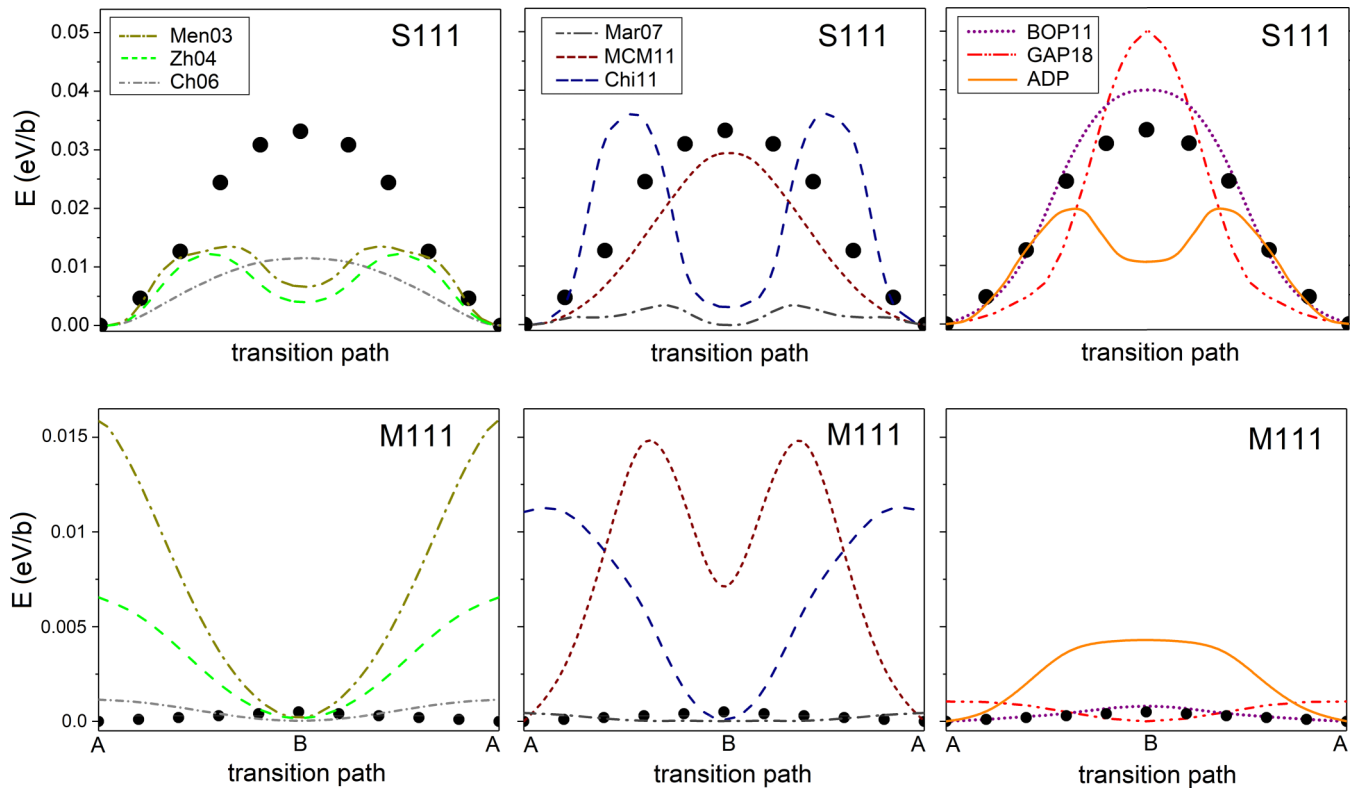
FIG. 11. The Peierls energy barriers for S111 and M111 dislocations. Black full circles show DFT results for screw dislocation from Ref. [26] and for mix dislocation (this work).

likely impossible to achieve for simplified potentials without a strong deterioration of other properties, as is obvious from the validation of the MCM11 model. One of the reasons of this difficulty are extremely small changes in the atomic energies

at variation in the dislocation barrier shape: the alternation in the barrier magnitude by 0.01 eV/b leads to the variation in the energy of the dislocation core atoms about 2 meV/atom. Such subtle variations in the energy landscape are difficult
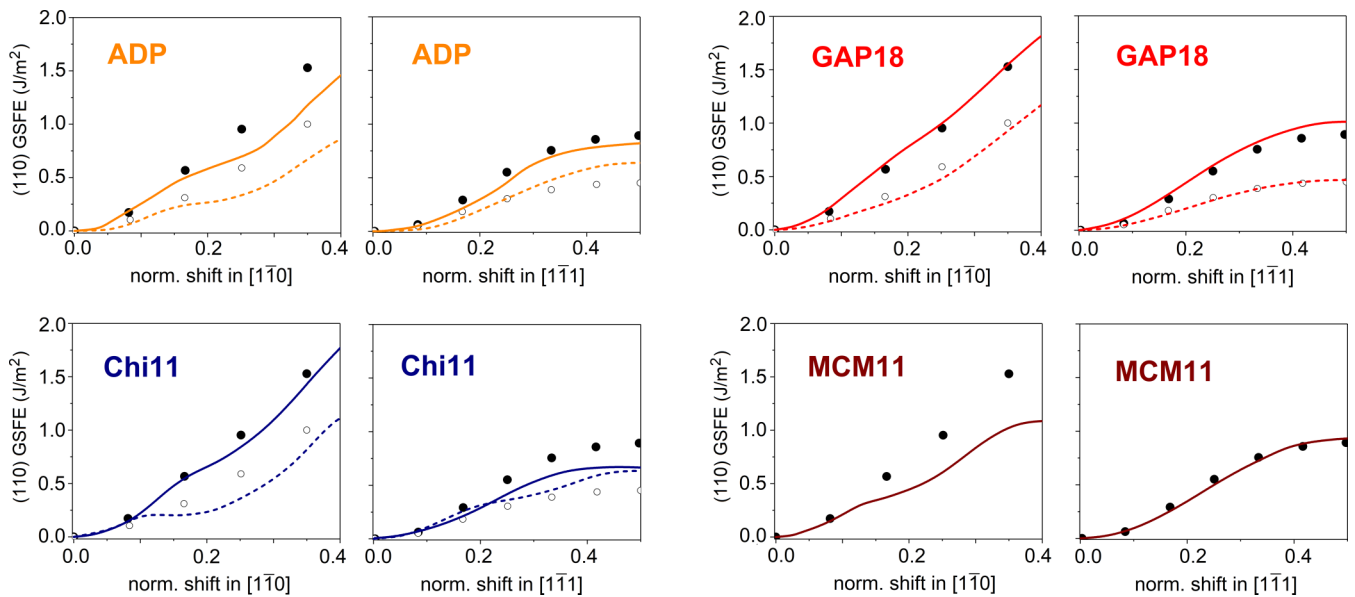

FIG. 12. GSFE of the (110) plane for shifts in $[1\bar{1}0]$ and $[1\bar{1}1]$ directions. Results for the unstrained crystal are shown by the solid line (potential calculations) and full circles (DFT) [121]. Calculations for the strained crystal (corresponding to 5% equibiaxial strain in [110] and $[1\bar{1}0]$ directions) are represented by the dashed line (potential) and empty circles (DFT) [121]. All GSFE curves are constructed with respect to the crystal energy at zero shift for a given crystal state.

to capture for a classical interatomic potential. Nevertheless, the impact of the barrier shape on the dislocation mobility at the finite temperature has not been studied in detail. Based on the results of several atomistic simulations of S111 dislocation behavior in bcc metals [118,122], the qualitatively incorrect barrier shape should not be critical for dislocation behavior at elevated temperatures.

Overall, GAP18 can be considered as the most quantitatively accurate model for description of defect properties in bcc Fe, but it has apparent transferability limitations for atomic configuration outside of its training database, such as for bulk phases under larger volumetric changes. In addition, GAP18 is computationally the most demanding of all tested models. Based on the performed comparisons, the developed ADP parametrization provides a reasonable balance between the accuracy and performance, which makes it attractive for large-scale MD simulations of defect behavior at finite temperatures [123–127].

V. APPLICATIONS OF OUR ADP POTENTIAL

In this section, we present several application examples that illustrate the predictive ability of the new ADP model in MD simulations at finite temperatures.

A. Phase stability at finite temperatures and pressures

To describe accurately the behavior of fcc Fe (γ-Fe) is a difficult task for classical potentials. The first prerequisite is an adequate representation of the bcc-fcc transformation and its corresponding energy landscape at zero temperature. To examine this transformation, it is convenient to consider the fcc and bcc lattices as particular cases of a body-centered tetragonal (bct) lattice characterized by two independent variables: Atomic volume (V) and the ratio of two lattice parameters (c/a). The well-known Bain path for the bcc-fcc martensitic transformation corresponds to the change of c/a from 1.0 (bcc) to $\sqrt{2}$ (fcc). Several DFT calculations [5,86,128] have revealed that the AFM and AFMD fcc phases (which are the lowest-energy fcc phases) are mechanically unstable at 0 K under the tetragonal distortion and transform to a tetragonal bct phase with the c/a ratio of about 1.5. A detailed study of the whole energy landscape for various magnetic orderings can be found in Ref. [86]. We performed similar calculations (without explicit magnetic interactions) for the tested potentials and plotted the results for several models in Fig. 13. We found that only GAP18 predicts the metastable bct structure but with $c/a = 1.71$, i.e., significantly more than the DFT value. ADP captures correctly the minimum energy path between the bcc and fcc structures while both Chi11 and MCM11 potentials show marked deviations of the energy landscape.

To examine the stability of the fcc phase at finite temperature, we performed a series of MD simulations at various temperatures and densities. As the AFM or AFMD magnetic order in the fcc phases may be considered as the first approximation for the paramagnetic state [86,129,130], temperature-induced changes of the magnetic disorder are likely to affect properties of the fcc phase less than those of the bcc phase. Hence, even classical potentials may achieve a
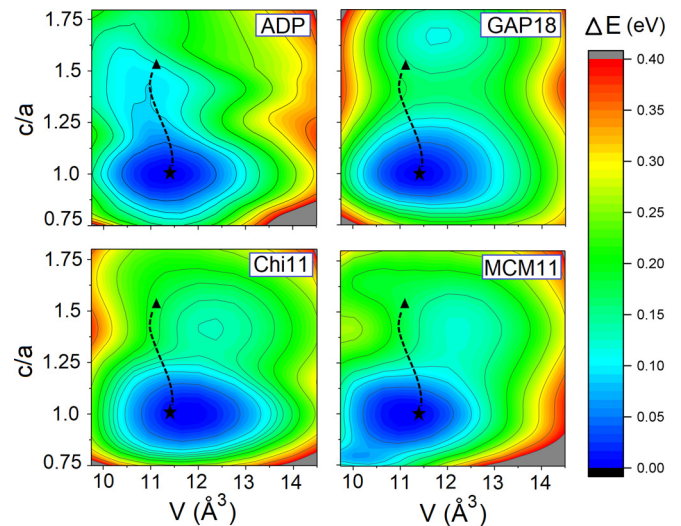

FIG. 13. The energy landscape for the bcc-fcc transformation in the $\{c/a, V\}$ space. Results of the DFT calculations [5,86] are marked by the star (bcc ground state), the triangle (metastable bct phase), and the dashed curve representing the minimum energy path between these two structures.

qualitatively correct representation of the fcc phase at elevated temperatures. Figure 14 shows the calculated $V(T)$ dependence obtained for isobaric heating and cooling of the fcc phase, initially equilibrated at $T = 1400$ K. The graph contains also the volume changes for the bcc phase obtained upon isobaric heating. The comparison of the ADP predictions with the experimental data [80,131] shows a qualitative agreement for the thermal expansion of both phases.

An interesting feature predicted by the ADP model is the existence of temperature- and volume-dependent lattice instabilities occurring in the fcc phase. As shown on the four
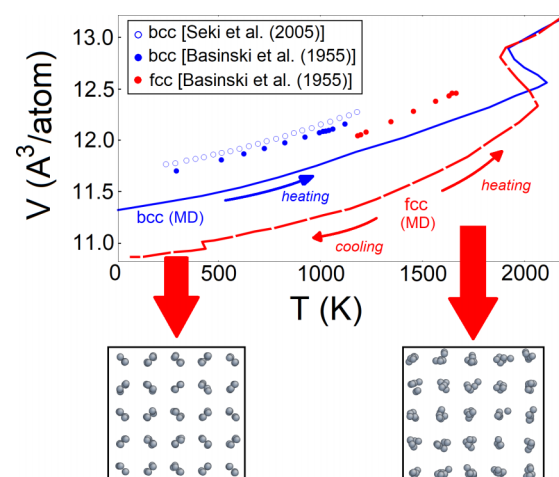

FIG. 14. The calculated dependence of atomic volume on temperature for the bcc phase (blue solid line) and for the fcc phase (red dashed line) from MD simulations performed at $P = 0$. The symbols mark available experimental data [80,131]. The MD snapshots illustrate lattice distortions of the fcc phase at low temperature (left bottom panel) and a stabilized fcc phase at elevated temperatures (right bottom panel).
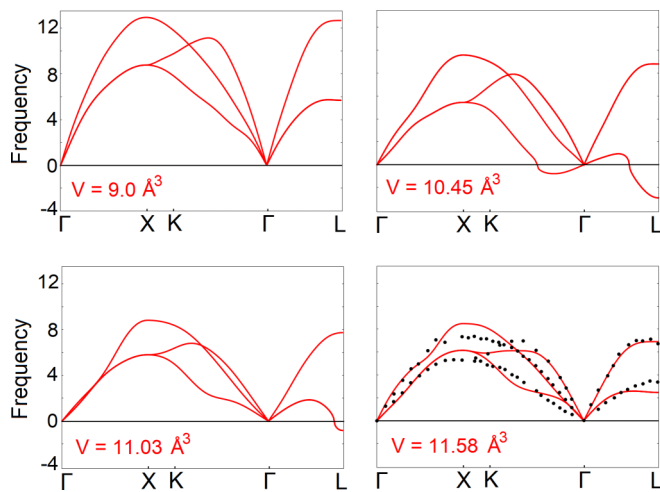
FIG. 15. Phonon dispersion curves for the fcc phase at various atomic volumes. The panel illustrating results for $V = 11.58$ Å contains also experimental data (black dots) obtained at $T = 1428$ K [132].

FIG. 16. The P-T phase diagram of Fe: Black lines, experimental data [87–89]; blue dotted line, DFT-based $\alpha \rightarrow \gamma$ transition line from Ref. [86]; red dashed-dotted lines, ADP predictions (the phase transition to ϵ phase is absent for the ADP model).

phonon dispersion plots in Fig. 15, the equilibrium ($V = 11.03$ Å) and moderately compressed ($V = 10.45$ Å) fcc phases exhibit a dynamical instability corresponding to the imaginary phonon frequencies near the L point. This instability occurs in MD simulations for $T < 400$ K and is visible on the MD snapshot in the bottom left panel of Fig. 14. The thermal expansion of the lattice for $T > 400$ K leads to disappearance of the imaginary frequencies and stabilization of the fcc phase. The phonon dispersion for the expanded lattice ($V = 11.58$ Å) agrees well with the experimental data [132]. Interestingly, a substantial hydrostatic compression also stabilizes the fcc phase (cf. top left panel of Fig. 15 for $V = 9.0$ Å). The large sensitivity of the phonon dispersion curves to volume variations for the Fe fcc phases has been reported by several DFT studies. However, while some studies revealed the presence of the imaginary frequencies in the AFM fcc phase at 0 K [133], others predicted their absence [129].

To obtain a complete picture of the phase stability, we computed the whole P-T phase diagram using the ADP model. The calculated results are presented in Fig. 16 together with the available experimental data [87–89] and DFT-based estimates [86]. The melting lines for both phases were evaluated for a wide range of pressures using the two-phase approach [134–136]. The melting temperatures for the bcc and fcc phases at zero pressure were estimated to be 1770 ± 10 K and 1640 ± 10 K, respectively. The pressure corresponding to the triple point for the bcc-fcc-liquid transition obtained from the intersection of the melting lines equals to 3.5 GPa. It is worth noting that the calculated melting line for γ-Fe agrees well with the measured data.

It is obvious that ADP does not predict the α-γ transition at zero pressure and the fcc phase remains metastable with respect to the bcc phase up to the melting. To estimate the transition temperature $T_{\alpha\gamma}$ for nonzero pressures, we used the Clausius-Clapeyron relation

$$\frac{dT_{\alpha\gamma}}{dP} = \frac{T_{\alpha\gamma} \Delta V}{\Delta H},$$
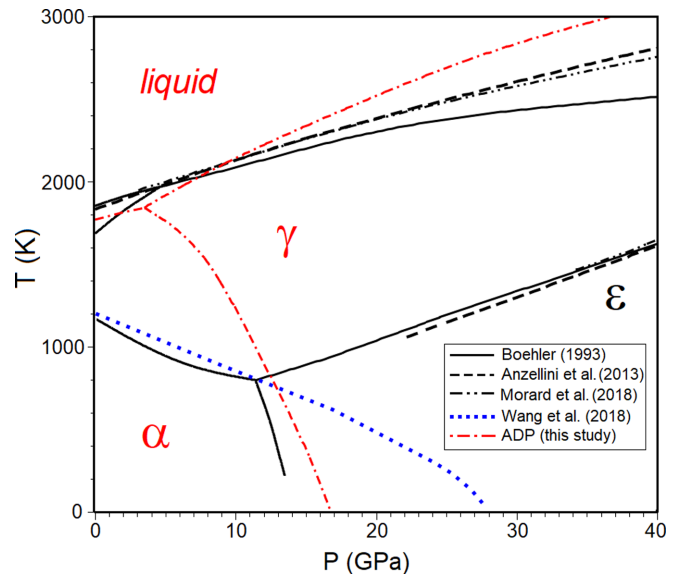
where ΔV and ΔH are the changes of volume and enthalpy at the phase transition. To integrate the equation, we first evaluated the enthalpies for both phases at $T = 0$ K and obtained the transition pressure $P_{\alpha\gamma}^{T=0} = 16.9$ GPa. By combining the information about the triple point, the transition pressure at $T = 0$ and the calculated dependencies $H(P, T)$ and $V(P, T)$ for both considered phases we obtain the α-γ stability line in Fig. 16.

Despite the lower stability of the fcc phase with respect to the bcc phase at zero pressure, the physical properties of the fcc phase at finite T are described with good accuracy. Table IV presents the ADP results in comparison with experimental values [80,132,137] and DFT predictions [129]. As we noted above, the magnetic interactions should affect the thermodynamic properties of the fcc phase much less than those of the bcc phase at elevated temperatures. A coupling of the ADP model with spin dynamics [16] may lead to an improved prediction of the $T_{\alpha\gamma}$ below T_m at zero pressure. This coupling as well as related questions about the transition between γ-Fe and δ-Fe (PM-bcc) will be a subject of future study.

TABLE IV. Properties of fcc phase at $T = 1500$ K. The simulation results obtained by ADP are compared with the experimental data [80,132,137] and DFT results [129].

	Experiment	DFT	ADP
a (Å)	3.66	3.61	3.60
C11 (GPa)	154	169	168
C12 (GPa)	122	105	130
C44 (GPa)	77	85	74
E_{vac}^{f} (eV)	1.7 ± 0.2		1.92
E_{SIA}^{f} (eV)			3.6

B. Spin dynamics

A possible way how to simulate α-Fe at high temperatures is to couple a classical interatomic potential with spin dynamics. Several approaches have been attempted so far. In a pioneering work, Ma *et al.* [15,16] used a potential fitted to reproduce the behavior of NM Fe that was augmented with a spin Hamiltonian in the Heisenberg-Landau form. The exchange coupling functions and the Landau coefficients of the Hamiltonian were adjusted to reproduce the properties of either bcc or fcc magnetic phases. Tranchida *et al.* [17] instead used a classical EAM potential fitted to reproduce the magnetic Fe phases and coupled it with SD after subtracting effectively the magnetic interactions. Very recently, they employed a similar strategy to fit simultaneously the magnetic interactions with a nonmagnetic ML potential [138]. This approach is perhaps more flexible than the coupling of SD with an interatomic potential fitted to the GM state, but it is also more sophisticated [16,138].

We have developed a nonmagnetic ADP potential (cf. Appendix A) that can be combined with the advanced SD modeling. In this work, however, we use the SD simulation based on the ADP model discussed in the previous section, which was fitted to reproduce the GM configurations. We applied the SD approach similar to that of Tranchida *et al.*, as realized in the LAMMPS code [17], to investigate the self-diffusion in bcc Fe (see also the following subsections). In this coupled approach, the atomic energy contains three different contributions:

$$U_i = U_{clas} - \sum_{j \neq i} J(r_{ij})(\mathbf{s_i s_j} - |s_i||s_j|), \qquad (6)$$

where the energy term U_{clas} is the classical contribution from our ADP potential and $J(r_{ij})$ is the exchange coupling between atomic spins $\mathbf{s_i}$ and $\mathbf{s_j}$ located on sites i and j, respectively. In this work, we used the function $J(r_{ij})$ offered in Ref. [139]. The dynamics of spins follows the Landau-Lifshitz-Gilbert equation [140].

The coupling of atomic and spin degrees of freedom in Eq. (6) allows to take into account the magnetic excitations as temperature increases. On the other hand, the simulated properties of bcc Fe at low temperature (approximately at $T < 0.5T_c$, where T_c is the Curie temperature) are only slightly affected by the SD contribution, as the second term in Eq. (6) approaches zero.

The combination of SD and MD gives a qualitative representation of Fe properties over a wide range of temperatures. Figure 17(a) illustrates the dependence of the total magnetic moment on temperature obtained from the SD simulation. The simulation results show a somewhat less abrupt reduction of the magnetic moment than in experiments due to the classical nature of the simulated magnetic subsystem. Nevertheless, the estimated Curie temperature for the simulated system (about 900 K) is close to the experimental value.

Figure 17(b) shows the dependence of specific heat (C_p) on temperature obtained using the coupled MD + SD simulations. The magnitude of C_p is significantly overestimated at low temperature because of the classical description of the magnetic subsystem. The value of C_p at $T < 600$ K should be less than 30 J/K/mol, due to the quantum suppression of
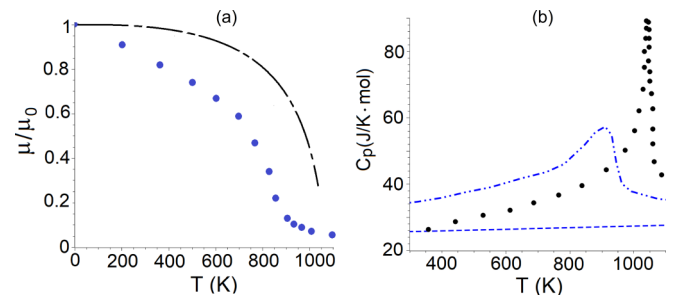

FIG. 17. The results of the coupled MD-SD simulations. (a) The dependence of the total magnetic moment on temperature (black dashed line, experimental data; blue points, simulation results). (b) The temperature dependence of specific heat (black dots, experimental data [141]; blue dashed line, MD simulation only; blue dashed-dotted-dotted line, MD + SD simulation).

the magnetic excitation [142], which is consistent with the predictions of the classical MD simulation. Nevertheless, the divergence of $C_p(T)$ near the Curie temperature is reproduced correctly.

It is important to note that the employed representation of the spin subsystem leads to several limitations. First and foremost, the spin magnitude is kept constant so no longitudinal spin fluctuations are considered in the model. Second, the exchange parameters $J(r_{ij})$ are also fixed and do not vary for different atomic environments. Hence, the MD + SD simulations of crystal defects are likely to provide only a qualitative description. Specifically, for the monovacancy in α-Fe, atomic spins around a vacancy differ only slightly from those in the bulk lattice while much larger variations of the spin magnitude are expected for interstitial defects, grain boundaries, or surfaces.

C. Self-diffusion in bcc and fcc Fe

The self-diffusion coefficient (D_{self}) may be considered as a product of vacancy concentration (c_{vac}) and single-vacancy diffusivity (D_{vac}). To study bulk diffusion in bcc Fe, we calculated the temperature dependencies of c_{vac} and D_{vac} by means of the combined MD + SD simulation using ADP. We performed also MD-only simulation of bulk self-diffusion in fcc Fe. The general methodology is similar to our recent study of self-diffusion in Mo [108].

As the first step, we carried out the MD simulation of the vacancy diffusion. The simulated supercells contained 1999 and 3999 atoms for the bcc and fcc phases, respectively. Each calculation was performed in the NVE ensemble, the volume was adjusted to obtain zero pressure. The value of D_{vac} was estimated from the squared displacements (δr_i^2) for all N atoms in the system during the simulation time t using the following equation:

$$D_{vac} = \sum_{i=1}^{N} \delta r_i^2 / 6t. \qquad (7)$$

A total MD time of 2 ns was found sufficient for a reliable determination of D_{vac} at high temperatures while lower temperatures required much longer times (of up to 30 ns) to achieve a sufficient number of jump events. The simulation
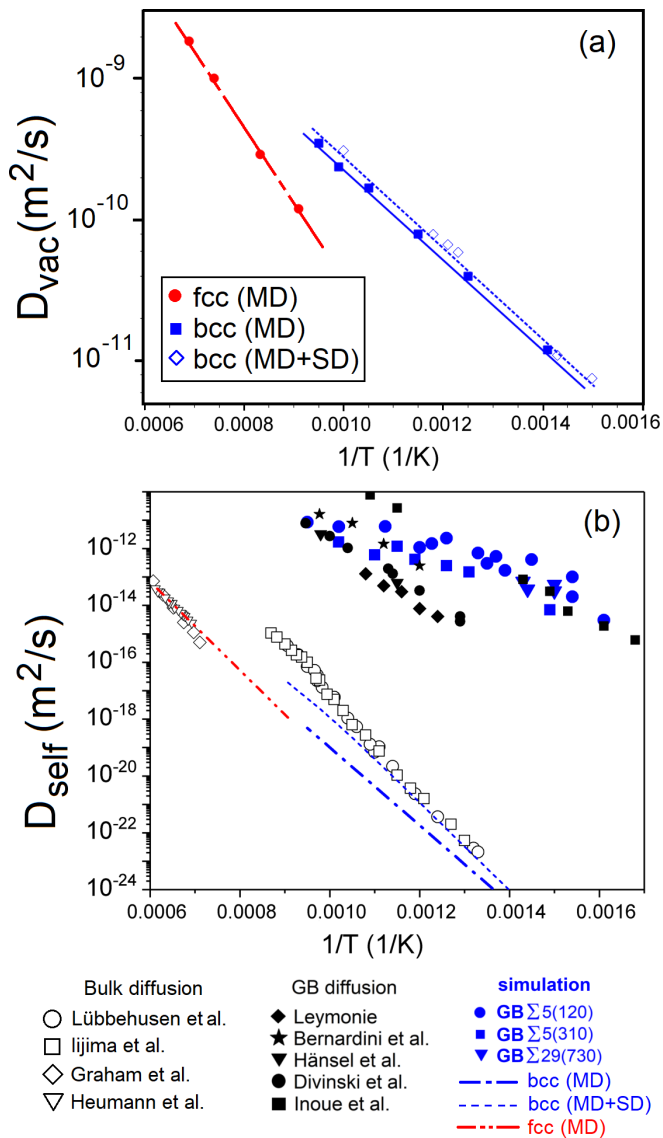
FIG. 18. (a) Diffusivity of a single vacancy in bcc and fcc lattices calculated at various temperatures. (b) Self-diffusion coefficients in different structures: the experimental data for bulk self-diffusion in bcc lattice [97,98] and fcc lattice [147,148] are shown by empty symbols; the experimental data for GB self-diffusion [149–153] are denoted by full black symbols; the lines correspond to the calculated bulk diffusion coefficients; full blue symbols indicate results of GB self-diffusion simulations.

cell). The value of $S_{vac}^f = 2.1\ k_B$, obtained as $S_{vac}^f = S_{vac} - S_{id}(431/432)$, agrees with the vacancy formation entropies calculated for other bcc metals [108,143]. For a metastable phase, such as fcc Fe, the calculation of S_{vac}^f requires more sophisticated methods. Thus, here we used $S_{vac}^f = 2.0\ k_B$ as this value lies in the range of entropies calculated for other fcc metals with comparable melting temperatures [144–146].

In the final part of this research, we calculated the vacancy formation energy at different temperatures in the spirit of our previous work [108]. The classical MD reproduced the temperature-independent values of E_{vac}^f for bcc and fcc Fe (2.05 end 1.92 eV). On the other hand, the coupled SD+MD simulations revealed a strong dependence of E_{vac}^f on T for α-Fe. At low temperatures ($T < 300$ K), the calculated $E_{vac}^f \approx 2.08$ eV is almost equal to the value calculated in classical MD. However, the spin disordering at heating causes a gradual increase of E_{vac}^f, with a maximum value of 2.39 eV at $T \approx 860$ K. Further heating leads to decrease in E_{vac}^f to 1.94 eV at $T \approx 1200$ K. This value may be considered as the vacancy formation energy in a PM state. Based on the performed calculations we estimated the vacancy concentration using the following equations:

$$c_{vac} = \exp\left[-F_{vac}(T)/k_B T\right],$$
$$F_{vac}^f = E_{vac}^f - T S_{vac}^f,$$

where F_{vac}^f is free energy of a vacancy. To trace the dependence $F_{vac}^f(T)$, we performed a thermodynamic integration based on the calculated E_{vac}^f at various temperatures (see work [108] for detailed description of the method).

Figure 18(b) shows the final summary of predicted self-diffusion coefficients $D_{self} = D_{vac} \exp\left[-F_{vac}^f(T)/k_B T\right]$. For fcc Fe, the obtained MD results agree well with the experimental data [147,148]. For bcc Fe, the lack of SD contribution leads to underestimated D_{self} compared to experiments [97,98]. As discussed above, the magnetic excitations lead to enhancement of the diffusion coefficient in the bcc phase (and deviations from the Arrhenius behavior) due to the temperature-dependent value of E_{vac}^f. It is clearly seen that the coupled MD + SD modeling allows to describe the experimental data on self-diffusion in α-Fe more accurately than pure classical MD. However, the perfect representation of self-diffusion in PM state was not achieved due to the limitations of the model.

In addition to bulk diffusion, we investigated also self-diffusion for several GBs in bcc Fe, similarly as in our recent study for other Fe potentials [103]. Such modeling demands to simulate approximately 50 000 atoms for $t \sim 10$ ns (10^7 steps). The results of the simulations using our ADP model are shown in Fig. 18(b) together with the available experimental data [149–153]. The ADP results are consistent with those of our previous work [103], namely, that the GB self-diffusion is mostly governed by self-interstitial atoms in contrast to the vacancy-mediated bulk diffusion.

D. Diffusion of SIA and diSIA

An important application of atomistic simulations is studies of radiation damage. We applied the ADP potential to

results are shown in Fig. 18(a). For the bcc phase, the slope of $D_{vac}(T)$ in Arrhenius coordinates is close to E_{vac}^m computed using NEB. Similar values of diffusion coefficients obtained in MD-only and MD + SD simulations indicate a small influence of the magnetic excitations on vacancy mobility, at least in the adopted SD model.

As the next step, we estimated the formation entropy of a vacancy S_{vac}^f in the bcc crystal at $T = 300$ K using the PHONOPY code [91]. This was done by computing phonon entropies for two different simulated systems: S_{id} for defectless crystal (with 432 atoms in a simulation cell) and S_{vac} for crystal containing a single vacancy (with 431 atoms in simulation

investigate the finite-T behavior of SIA and di-SIA defects, which are known to play a key role in the irradiated materials [25,95].

Irradiation of a material and subsequent annealing accompanied by measurements of electrical resistivity recovery can provide primary information about key processes related to defect migration. According to the pioneering work of Takaki *et al.* [154], it is possible to identify several basic stages of the resistivity recovery in α-Fe. For the current discussion, two stages are especially important: I_E and I_2 taking place at $T = 124\text{--}144$ K and $T = 164\text{--}185$ K, respectively. The I_E stage was attributed to the recombination of uncorrelated Frenkel pairs (consisting of SIA and vacancy). Thus, the activation energy associated with the stage I_E is interpreted as the migration energy of SIA. The I_2 stage was explained to be related to the di-SIA migration. The following migration energies were originally proposed [154]: 0.27 ± 0.04 eV and 0.42 ± 0.03 for the migration of SIA and di-SIA, respectively. A compilation of additional measurements [155,156] leads to a more precise estimation for the SIA migration energy: $E_{\text{SIA}}^m = 0.30 \pm 0.02$ eV.

The SIA diffusion in bcc Fe is expected to take place via a translation-rotation nearest-neighbor jump mechanism proposed by Johnson [157]. DFT calculations [158,159] predict a slightly overestimated value of $E_{\text{SIA}}^m = 0.34$ eV in comparison with the experimental data while most classical interatomic potentials underestimate the migration barrier [25,160,161]. Only three classical potentials, namely, Men03, Mar07, and Chi11, predict the SIA migration energy to be about 0.30 ± 0.01 eV [25,26].

We performed several MD simulations using ADP to investigate the diffusion of a single SIA defect in a cubic supercell containing 687 atoms. The diffusion coefficient for a given temperature was estimated from the squared displacement of the SIA defect tracked during the calculation run. The obtained simulation results are shown in Fig. 19(a). The calculated E_{SIA}^m for the ADP model equals 0.17 ± 0.01 eV. Even though the potential underestimates the migration energy, it correctly reproduces the diffusion mechanism proposed by Johnson [157].

The diffusion of di-SIA is much less studied than the SIA diffusion. As discussed above, the DFT calculations [5,25] revealed that the most stable state of di-SIA is the non-parallel NPC configuration. Unfortunately, to investigate the migration of this di-SIA configuration is computationally too demanding for DFT. MD simulations were also not able to shed light on the diffusion details because almost all classical potentials do not predict the NPC but the $\langle 110 \rangle$ dumbbell configuration as the di-SIA ground state. In some cases, such shortcoming leads to a higher mobility of di-SIA than SIA mobility [162]. Among all models tested in this work, only MCM11, ADP, and GAP18 potentials predict correctly the energy hierarchy of di-SIA configurations. For ADP, the energy difference between the two lowest di-SIA configurations is equal to 0.07 eV, which is close to the DFT results [25].

The computed temperature dependence of the di-SIA diffusion coefficient is plotted in Fig. 19(a). In addition, Fig. 19(b) presents an example of the squared displacements as a function of time. It is interesting to note that the di-SIA diffusion may be considered as a combination of thermally activated
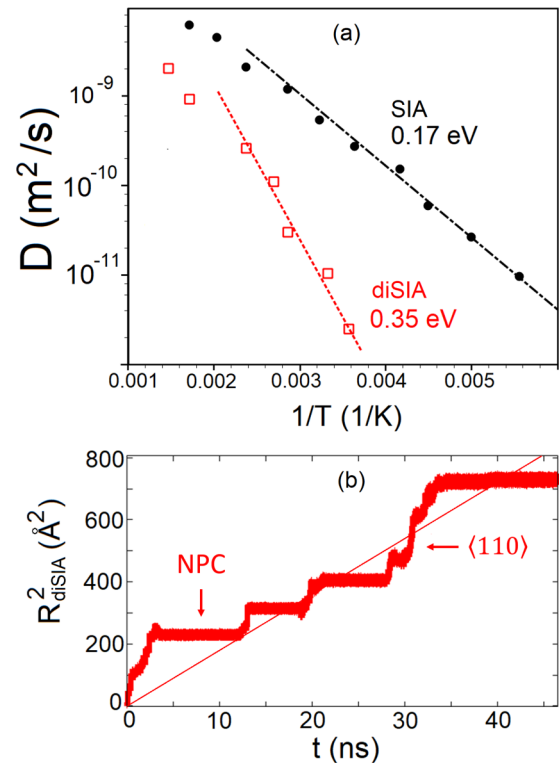

FIG. 19. SIA and di-SIA diffusion in α-Fe. (a) Calculated diffusion coefficients of SIA and di-SIA at different temperatures. The values of migration energies at low temperature are listed as well. (b) The squared displacement of di-SIA at $T = 350$ K. The arrows indicate configurations of the defect in the NPC and $\langle 110 \rangle$ states.

transition from NPC to the $\langle 110 \rangle$ configuration, and migration of the latter one. The estimated migration energy of di-SIA equals to 0.35 eV, which is close to the experimental estimation.

The performed MD simulations reveal that the ADP can qualitatively reproduce the behavior of interstitial defects at finite temperatures. Despite the underestimation of E_{SIA}^m, our model predicts correct diffusion mechanisms and shows a reasonable difference between the migration energies of the point defects.

VI. CONCLUSION

In this work, we presented an angular-dependent interatomic potential developed primarily for large-scale atomistic simulations of crystal defects in Fe. The aim was to utilize advanced fitting techniques to optimize the potential parameters based on large training set of DFT energies and forces to achieve the best balance between accuracy and computational efficiency. We carried out a detailed validation of the developed model together with a number of other potentials for Fe in order to critically assess the application range and limitations of each model.

This validation clearly showed that despite extensive effort in the past decades, there exists no universally applicable interatomic potential for Fe. Even sophisticated models such as tight-binding based magnetic BOP, which contains an explicit treatment of magnetic interactions, or machine-learned GAP,

which was trained on a large DFT data set, do have limitations. Despite not being perfect, the ADP potential provides a robust description for a broad range of properties of bulk iron as well as its crystal defects while allowing to carry out large-scale MD simulations up to 10^7 atoms and 100 ns. Our future activities will focus on the coupling of classical and spin dynamics as well as further extensions to multicomponent systems [163].

ACKNOWLEDGMENTS

APPENDIX A

In this Appendix, we present another ADP parametrization for description of Fe in the NM state. The construction was generally the same as for ADP potential in the GM state, with the differences only in the reference data. The reference forces used for the fitting of the NM potential are reproduced with a similar accuracy as for the GM potential in Fig. 2. The main purpose of the NM potential is its coupling with the spin-dynamics simulations where the dynamics of atoms is described by the ADP potential while the spin interactions are treated by the SD equations [15,16]. In this coupled simulation, the energy of the atomic system is described as a combination of magnetic (M) and nonmagnetic (NM) contributions: $U = U_{NM} + U_M$.

Figure 20 shows the *E-V* curves for several NM phases obtained by the NM ADP potential and DFT calculations. The cohesive energy of the NM fcc phase is equal to 4.18 eV/atom. The calculated *E-V* curves agree well with the reference DFT results [10,23]. This potential can be downloaded from NIST database of interatomic potentials [64,65] just like the ADP potential for the GM state. In addition to the spin-dynamics simulation, the joint use of the two developed angular-dependent potentials allows to estimate magnetic energy of various crystal defects and states. A comparison between the energies calculated for the same atomic
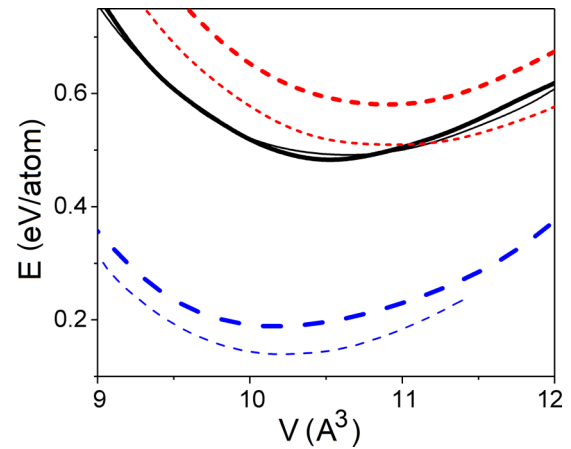

FIG. 20. Energy-volume curves for different NM phases (energies are plotted with respect to the ground energy of the FM bcc phase): Blue dashed lines, fcc; solid black lines, bcc; red short dashed lines, C15. Thick and thin lines correspond to NM ADP and DFT [10,23], respectively.

configuration in GM and NM states allows to estimate the magnetic contribution in the energy.

APPENDIX B

Figure 21 illustrates $E(V)$ curves for four interatomic potentials over a broad range of volumes. The low cohesive energy of the GAP18 model originates from the nonphysical behavior at $V > 15$ Å^3/atom.
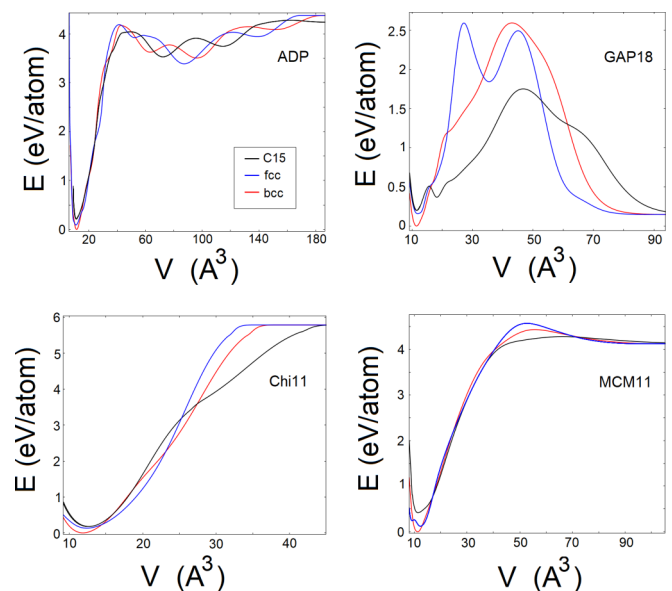

FIG. 21. The energy-volume curves for four interatomic models over a broad range of volumes.

[1] R. Johnson and D. Oh, Analytic embedded atom method model for bcc metals, J. Mater. Res. **4**, 1195 (1989).

[2] R. Drautz and D. G. Pettifor, Valence-dependent analytic bond-order potential for magnetic transition metals, Phys. Rev. B **84**, 214114 (2011).

[3] L. V. Pourovskii, J. Mravlje, M. Ferrero, O. Parcollet, and I. A. Abrikosov, Impact of electronic correlations on the equation of state and transport in ε-Fe, Phys. Rev. B **90**, 155120 (2014).

[4] T. Schickling, J. Bünemann, F. Gebhard, and L. Boeri, Quasiparticle bands and structural phase transition of iron from gutzwiller density-functional theory, Phys. Rev. B **93**, 205151 (2016).

[5] D. Dragoni, T. D. Daff, G. Csányi, and N. Marzari, Achieving DFT accuracy with a machine-learning interatomic potential: Thermomechanics and defects in bcc ferromagnetic iron, Phys. Rev. Mater. **2**, 013808 (2018).

[6] D. G. Pettifor, *Bonding and Structure of Molecules and Solids* (Oxford University Press, Oxford, 1995).

[7] P.-W. Ma and S. L. Dudarev, Universality of point defect structure in body-centered cubic metals, Phys. Rev. Mater. **3**, 013605 (2019).

[8] J. B. Chapman, P.-W. Ma, and S. L. Dudarev, Effect of non-heisenberg magnetic interactions on defects in ferromagnetic iron, Phys. Rev. B **102**, 224106 (2020).

[9] M.-C. Marinica, F. Willaime, and J.-P. Crocombette, Irradiation-Induced Formation of Nanocrystallites with C15 Laves Phase Structure in BCC Iron, Phys. Rev. Lett. **108**, 025501 (2012).

[10] L. Dézerald, M.-C. Marinica, L. Ventelon, D. Rodney, and F. Willaime, Stability of self-interstitial clusters with C15 laves phase structure in iron, J. Nucl. Mater. **449**, 219 (2014).

[11] R. Alexander, M.-C. Marinica, L. Proville, F. Willaime, K. Arakawa, M. R. Gilbert, and S. L. Dudarev, *Ab initio* scaling laws for the formation energy of nanosized interstitial defect clusters in iron, tungsten, and vanadium, Phys. Rev. B **94**, 024103 (2016).

[12] H. Wen, P.-W. Ma, and C. Woo, Spin-lattice dynamics study of vacancy formation and migration in ferromagnetic bcc iron, J. Nucl. Mater. **440**, 428 (2013).

[13] D. Gambino and B. Alling, Lattice relaxations in disordered Fe-based materials in the paramagnetic state from first principles, Phys. Rev. B **98**, 064105 (2018).

[14] A. Schneider, C.-C. Fu, F. Soisson, and C. Barreteau, Atomic Diffusion in α-Iron Across the Curie Point: An Efficient and Transferable *ab Initio*–Based Modeling Approach, Phys. Rev. Lett. **124**, 215901 (2020).

[15] P.-W. Ma, C. H. Woo, and S. L. Dudarev, Large-scale simulation of the spin-lattice dynamics in ferromagnetic iron, Phys. Rev. B **78**, 024434 (2008).

[16] P.-W. Ma, S. L. Dudarev, and J. S. Wróbel, Dynamic simulation of structural phase transitions in magnetic iron, Phys. Rev. B **96**, 094418 (2017).

[17] J. Tranchida, S. Plimpton, P. Thibaudeau, and A. Thompson, Massively parallel symplectic algorithm for coupled magnetic spin dynamics and molecular dynamics, J. Comput. Phys. **372**, 406 (2018).

[18] G. Ackland, D. Bacon, A. Calder, and T. Harry, Computer simulation of point defect properties in dilute Fe-Cu alloy using a many-body interatomic potential, Philos. Mag. A **75**, 713 (1997).

[19] M. Mendelev, S. Han, D. Srolovitz, G. Ackland, D. Sun, and M. Asta, Development of new interatomic potentials appropriate for crystalline and liquid iron, Philos. Mag. **83**, 3977 (2003).

[20] X. W. Zhou, R. A. Johnson, and H. N. G. Wadley, Misfit-energy-increasing dislocations in vapor-deposited CoFe/NiFe multilayers, Phys. Rev. B **69**, 144113 (2004).

[21] H. Chamati, N. Papanicolaou, Y. Mishin, and D. Papaconstantopoulos, Embedded-atom potential for Fe and its application to self-diffusion on Fe(100), Surf. Sci. **600**, 1793 (2006).

[22] L. Sandoval, H. M. Urbassek, and P. Entel, Solid-solid phase transitions and phonon softening in an embedded-atom method model for iron, Phys. Rev. B **80**, 214108 (2009).

[23] M. Müller, P. Erhart, and K. Albe, Analytic bond-order potential for bcc and fcc iron-comparison with established embedded-atom method potentials, J. Phys.: Condens. Matter **19**, 326220 (2007).

[24] P. A. Olsson, Semi-empirical atomistic study of point defect properties in bcc transition metals, Comput. Mater. Sci. **47**, 135 (2009).

[25] L. Malerba, M.-C. Marinica, N. Anento, C. Björkas, H. Nguyen, C. Domain, F. Djurabekova, P. Olsson, K. Nordlund, A. Serra *et al.*, Comparison of empirical interatomic potentials for iron applied to radiation damage studies, J. Nucl. Mater. **406**, 19 (2010).

[26] S. Chiesa, P. Derlet, S. Dudarev, and H. Van Swygenhoven, Optimization of the magnetic potential for α-Fe, J. Phys.: Condens. Matter **23**, 206001 (2011).

[27] L. Proville, D. Rodney, and M.-C. Marinica, Quantum effect on thermally activated glide of dislocations, Nat. Mater. **11**, 845 (2012).

[28] E. Asadi, M. AsleZaeem, S. Nouranian, and M. I. Baskes, Quantitative modeling of the equilibration of two-phase solid-liquid Fe by atomistic simulations on diffusive time scales, Phys. Rev. B **91**, 024105 (2015).

[29] S. A. Etesami and E. Asadi, Molecular dynamics for near melting temperatures simulations of metals using modified embedded-atom method, J. Phys. Chem. Solids **112**, 61 (2018).

[30] J. J. Möller and E. Bitzek, Comparative study of embedded atom potentials for atomistic simulations of fracture in α-iron, Modell. Simul. Mater. Sci. Eng. **22**, 045002 (2014).

[31] M. Mrovec, D. Nguyen-Manh, C. Elsässer, and P. Gumbsch, Magnetic Bond-Order Potential for Iron, Phys. Rev. Lett. **106**, 246402 (2011).

[32] Z. Chen, M. Mrovec, and P. Gumbsch, Atomistic aspects of screw dislocation behavior in α-iron and the derivation of microscopic yield criterion, Modell. Simul. Mater. Sci. Eng. **21**, 055023 (2013).

[33] Y.-S. Lin, M. Mrovec, and V. Vitek, Bond-order potential for magnetic body-centered-cubic iron and its transferability, Phys. Rev. B **93**, 214107 (2016).

[34] A. P. Bartók, M. C. Payne, R. Kondor, and G. Csányi, Gaussian Approximation Potentials: The Accuracy of Quantum Mechanics, without the Electrons, Phys. Rev. Lett. **104**, 136403 (2010).

[35] Y. Zuo, C. Chen, X. Li, Z. Deng, Y. Chen, J. Behler, G. Csányi, A. V. Shapeev, A. P. Thompson, M. A. Wood *et al.*, Performance and cost assessment of machine learning interatomic potentials, J. Phys. Chem. A **124**, 731 (2020).

[36] H. Mori and T. Ozaki, Neural network atomic potential to investigate the dislocation dynamics in bcc iron, Phys. Rev. Mater. **4**, 040601(R) (2020).

[37] M. R. Fellinger, A. M. Z. Tan, L. G. Hector, Jr., and D. R. Trinkle, Geometries of edge and mixed dislocations in bcc Fe from first-principles calculations, Phys. Rev. Mater. **2**, 113605 (2018).

[38] J. Byggmästar, K. Nordlund, and F. Djurabekova, Gaussian approximation potentials for body-centered-cubic transition metals, Phys. Rev. Mater. **4**, 093802 (2020).

[39] C. de Tomas, A. Aghajamali, J. L. Jones, D. J. Lim, M. J. López, I. Suarez-Martinez, and N. A. Marks, Transferability in interatomic potentials for carbon, Carbon **155**, 624 (2019).

[40] Y. Lysogorskiy, C van der Oord, A. Bochkarev, S. Menon, M. Rinaldi, T. Hammerschmidt, M. Mrovec, A. Thompson, G. Csányi, C. Ortner, and R. Drautz, Performant implementation of the atomic cluster expansion (PACE): Application to copper and silicon, arXiv:2103.00814v1.

[41] C. Huang, X. Peng, T. Fu, X. Chen, H. Xiang, Q. Li, and N. Hu, Molecular dynamics simulation of bcc Ta with coherent twin boundaries under nanoindentation, Mater. Sci. Eng.: A **700**, 609 (2017).

[42] L. A. Zepeda-Ruiz, A. Stukowski, T. Oppelstrup, and V. V. Bulatov, Probing the limits of metal plasticity with molecular dynamics simulations, Nature (London) **550**, 492 (2017).

[43] Z. Zhao and F. Chu, Atomic behaviors of crack propagation in bcc iron under dynamic loading rate with rectangular fluctuation, Mater. Sci. Eng.: A **707**, 81 (2017).

[44] Y. Shibuta, M. Ohno, and T. Takaki, Solidification in a supercomputer: From crystal nuclei to dendrite assemblages, JOM **67**, 1793 (2015).

[45] Y. Shibuta, K. Oguchi, T. Takaki, and M. Ohno, Homogeneous nucleation and microstructure evolution in million-atom molecular dynamics simulation, Sci. Rep. **5**, 13534 (2015).

[46] S. Okita, E. Miyoshi, S. Sakane, T. Takaki, M. Ohno, and Y. Shibuta, Grain growth kinetics in submicrometer-scale molecular dynamics simulation, Acta Mater. **153**, 108 (2018).

[47] Y. Shibuta, K. Oguchi, and T. Suzuki, Large-scale molecular dynamics study on evolution of grain boundary groove of iron, ISIJ Int. **52**, 2205 (2012).

[48] Y. Zhang, G. J. Tucker, and J. R. Trelewicz, Stress-assisted grain growth in nanocrystalline metals: Grain boundary mediated mechanisms and stabilization through alloying, Acta Mater. **131**, 39 (2017).

[49] P. A. Romero, T. T. Järvi, N. Beckmann, M. Mrovec, and M. Moseler, Coarse Graining and Localized Plasticity between Sliding Nanocrystalline Metals, Phys. Rev. Lett. **113**, 036101 (2014).

[50] B. Beeler, M. Asta, P. Hosemann, and N. Grønbech-Jensen, Effects of applied strain on radiation damage generation in body-centered cubic iron, J. Nucl. Mater. **459**, 159 (2015).

[51] K. Zolnikov, A. Korchuganov, and D. Kryzhevich, Molecular dynamics simulation of primary radiation damage in Fe–Cr alloy, J. Phys.: Conf. Ser. **774**, 012130 (2016).

[52] A. E. Sand, M. Aliaga, M. J. Caturla, and K. Nordlund, Surface effects and statistical laws of defects in primary radiation damage: Tungsten vs. iron, Europhys. Lett. **115**, 36001 (2016).

[53] Q. Peng, F. Meng, Y. Yang, C. Lu, H. Deng, L. Wang, S. De, and F. Gao, Shockwave generates 100 dislocation loops in bcc iron, Nat. Commun. **9**, 4880 (2018).

[54] J. Byggmästar, F. Granberg, A. E. Sand, A. Pirttikoski, R. Alexander, M. Marinica, and K. Nordlund, Collision cascades overlapping with self-interstitial defect clusters in Fe and W, J. Phys.: Condens. Matter **31**, 245402 (2019).

[55] G. P. Pun, R. Batra, R. Ramprasad, and Y. Mishin, Physically informed artificial neural networks for atomistic modeling of materials, Nat. Commun. **10**, 2339 (2019).

[56] Y.-S. Lin, G. P. P. Pun, and Y. Mishin, Development of a physically-informed neural network interatomic potential for tantalum, arXiv:2101.06540.

[57] F. Ercolessi and J. B. Adams, Interatomic potentials from first-principles calculations: The force-matching method, Europhys. Lett. **26**, 583 (1994).

[58] M. S. Daw and M. I. Baskes, Embedded-atom method: Derivation and application to impurities, surfaces, and other defects in metals, Phys. Rev. B **29**, 6443 (1984).

[59] S. Starikov, L. Kolotova, A. Y. Kuksin, D. Smirnova, and V. Tseplyaev, Atomistic simulation of cubic and tetragonal phases of U-Mo alloy: Structure and thermodynamic properties, J. Nucl. Mater. **499**, 451 (2018).

[60] V. Tseplyaev and S. Starikov, The atomistic simulation of pressure-induced phase transition in uranium mononitride, J. Nucl. Mater. **480**, 7 (2016).

[61] R. C. Ehemann and J. W. Wilkins, Force-matched empirical potential for martensitic transitions and plastic deformation in Ti-Nb alloys, Phys. Rev. B **96**, 184105 (2017).

[62] D. Smirnova, S. Starikov, and A. Vlasova, New interatomic potential for simulation of pure magnesium and magnesium hydrides, Comput. Mater. Sci. **154**, 295 (2018).

[63] W. Setyawan, N. Gao, and R. J. Kurtz, A tungsten-rhenium interatomic potential for point defect studies, J. Appl. Phys. **123**, 205102 (2018).

[64] C. A. Becker, F. Tavazza, Z. T. Trautt, and R. A. B. de Macedo, Considerations for choosing and using force fields and interatomic potentials in materials science and engineering, Curr. Opin. Solid State Mater. Sci. **17**, 277 (2013).

[65] L. M. Hale, Z. T. Trautt, and C. A. Becker, Evaluating variability with atomistic simulations: The effect of potential and calculation methodology on the modeling of lattice and elastic constants, Modell. Simul. Mater. Sci. Eng. **26**, 055003 (2018).

[66] S. Plimpton, Fast parallel algorithms for short-range molecular dynamics, J. Comput. Phys. **117**, 1 (1995).

[67] E. B. Tadmor, R. S. Elliott, J. P. Sethna, R. E. Miller, and C. A. Becker, The potential of atomistic simulations and the knowledgebase of interatomic models, JOM **63**, 17 (2011).

[68] M. Finnis and J. Sinclair, A simple empirical n-body potential for transition metals, Philos. Mag. A **50**, 45 (1984).

[69] Y.-S. Lin, M. Mrovec, and V. Vitek, A new method for development of bond-order potentials for transition bcc metals, Modell. Simul. Mater. Sci. Eng. **22**, 034002 (2014).

[70] Y. Mishin, M. Mehl, and D. Papaconstantopoulos, Phase stability in the Fe-Ni system: Investigation by first-principles calculations and atomistic simulations, Acta Mater. **53**, 4029 (2005).

[71] M. I. Baskes, J. S. Nelson, and A. F. Wright, Semiempirical modified embedded-atom potentials for silicon and germanium, Phys. Rev. B **40**, 6085 (1989).

[72] D. Smirnova, A. Y. Kuksin, and S. Starikov, Investigation of point defects diffusion in bcc uranium and u–mo alloys, J. Nucl. Mater. **458**, 304 (2015).

[73] P. Brommer and F. Gähler, Potfit: Effective potentials from *ab initio* data, Modell. Simul. Mater. Sci. Eng. **15**, 295 (2007).

[74] P. Brommer, A. Kiselev, D. Schopf, P. Beck, J. Roth, and H.-R. Trebin, Classical interaction potentials for diverse materials from *ab initio* data: A review of potfit, Modell. Simul. Mater. Sci. Eng. **23**, 074002 (2015).

[75] G. Kresse and J. Furthmüller, Efficient iterative schemes for *ab initio* total-energy calculations using a plane-wave basis set, Phys. Rev. B **54**, 11169 (1996).

[76] J. P. Perdew, K. Burke, and M. Ernzerhof, Generalized Gradient Approximation Made Simple, Phys. Rev. Lett. **77**, 3865 (1996).

[77] See Supplemental Material at http://link.aps.org/supplemental/10.1103/PhysRevMaterials.5.063607 for cubic spline parameters of developed ADP potential.

[78] D. Sherrington, Spin glasses, Phys. Bull. **30**, 477 (1979).

[79] E. Bonetti, L. Del Bianco, D. Fiorani, D. Rinaldi, R. Caciuffo, and A. Hernando, Disordered Magnetism at the Grain Boundary of Pure Nanocrystalline Iron, Phys. Rev. Lett. **83**, 2829 (1999).

[80] Z. S. Basinski, W. Hume-Rothery, and A. Sutton, The lattice expansion of iron, Proc. R. Soc. London, Ser. A **229**, 459 (1955).

[81] C. Kittel, *Introduction to Solid State Physics* (Wiley, New York, 1966).

[82] J. J. Adams, D. Agosta, R. Leisure, and H. Ledbetter, Elastic constants of monocrystal iron from 3 to 500 K, J. Appl. Phys. **100**, 113530 (2006).

[83] Y. Liu, F. Sommer, and E. Mittemeijer, Calibration of the differential dilatometric measurement signal upon heating and cooling; thermal expansion of pure iron, Thermochim. Acta **413**, 215 (2004).

[84] D. Dragoni, D. Ceresoli, and N. Marzari, Thermoelastic properties of α-iron from first-principles, Phys. Rev. B **91**, 104105 (2015).

[85] T. Hammerschmidt, B. Seiser, M. E. Ford, A. Ladines, S. Schreiber, N. Wang, J. Jenke, Y. Lysogorskiy, C. Teijeiro, M. Mrovec *et al.*, Bopfox program for tight-binding and analytic bond-order potential calculations, Comput. Phys. Commun. **235**, 221 (2019).

[86] K. Wang, S.-L. Shang, Y. Wang, Z.-K. Liu, and F. Liu, Martensitic transition in Fe via bain path at finite temperatures: A comprehensive first-principles study, Acta Mater. **147**, 261 (2018).

[87] R. Boehler, Temperatures in the earth's core from melting-point measurements of iron at high static pressures, Nature (London) **363**, 534 (1993).

[88] G. Morard, S. Boccato, A. D. Rosa, S. Anzellini, F. Miozzi, L. Henry, G. Garbarino, M. Mezouar, M. Harmand, F. Guyot *et al.*, Solving controversies on the iron phase diagram under high pressure, Geophys. Res. Lett. **45**, 11 (2018).

[89] S. Anzellini, A. Dewaele, M. Mezouar, P. Loubeyre, and G. Morard, Melting of iron at earth's inner core boundary based on fast x-ray diffraction, Science **340**, 464 (2013).

[90] L. B. Pártay, On the performance of interatomic potential models of iron: Comparison of the phase diagrams, Comput. Mater. Sci. **149**, 153 (2018).

[91] A. Togo and I. Tanaka, First principles phonon calculations in materials science, Scr. Mater. **108**, 1 (2015).

[92] B. Brockhouse, H. Abou-Helal, and E. Hallman, Lattice vibrations in iron at 296 K, Solid State Commun. **5**, 211 (1967).

[93] P.-W. Ma and S. L. Dudarev, Effect of stress on vacancy formation and migration in body-centered-cubic metals, Phys. Rev. Mater. **3**, 063601 (2019).

[94] G. Henkelman and H. Jónsson, Improved tangent estimate in the nudged elastic band method for finding minimum energy paths and saddle points, J. Chem. Phys. **113**, 9978 (2000).

[95] C.-C. Fu, J. Dalla Torre, F. Willaime, J.-L. Bocquet, and A. Barbu, Multiscale modelling of defect kinetics in irradiated iron, Nat. Mater. **4**, 68 (2005).

[96] D. Costa, G. Adjanor, C. Becquart, P. Olsson, and C. Domain, Vacancy migration energy dependence on local chemical environment in Fe–Cr alloys: A density functional theory study, J. Nucl. Mater. **452**, 425 (2014).

[97] Y. Iijima, K. Kimura, and K. Hirano, Self-diffusion and isotope effect in α-iron, Acta Metall. **36**, 2811 (1988).

[98] M. Lübbehusen and H. Mehrer, Self-diffusion in α-iron: The influence of dislocations and the effect of the magnetic phase transition, Acta Metall. Mater. **38**, 283 (1990).

[99] D. A. Terentyev, T. P. C. Klaver, P. Olsson, M.-C. Marinica, F. Willaime, C. Domain, and L. Malerba, Self-Trapped Interstitial-Type Defects in Iron, Phys. Rev. Lett. **100**, 145503 (2008).

[100] L. Malerba, G. Ackland, C. Becquart, G. Bonny, C. Domain, S. L. Dudarev, C.-C. Fu, D. Hepburn, M.-C. Marinica, P. Olsson *et al.*, *Ab initio* calculations and interatomic potentials for iron and iron alloys: Achievements within the perfect project, J. Nucl. Mater. **406**, 7 (2010).

[101] Y. Zhang, X.-M. Bai, M. R. Tonks, and S. B. Biner, Formation of prismatic loops from c15 laves phase interstitial clusters in body-centered cubic iron, Scr. Mater. **98**, 5 (2015).

[102] L. Ventelon, F. Willaime, C.-C. Fu, M. Heran, and I. Ginoux, *Ab initio* investigation of radiation defects in tungsten: Structure of self-interstitials and specificity of di-vacancies compared to other bcc transition metals, J. Nucl. Mater. **425**, 16 (2012).

[103] S. Starikov, M. Mrovec, and R. Drautz, Study of grain boundary self-diffusion in iron with different atomistic models, Acta Mater. (unpublished).

[104] J. Wang, G. K. Madsen, and R. Drautz, Grain boundaries in bcc-fe: A density-functional theory and tight-binding study, Modell. Simul. Mater. Sci. Eng. **26**, 025008 (2018).

[105] H. Lambert, A. Fekete, J. R. Kermode, and A. De Vita, Imeall: A computational framework for the calculation of the atomistic properties of grain boundaries, Comput. Phys. Commun. **232**, 256 (2018).

[106] M. I. Mendelev, H. Zhang, and D. J. Srolovitz, Grain boundary self-diffusion in ni: Effect of boundary inclination, J. Mater. Res. **20**, 1146 (2005).

[107] T. Frolov and Y. Mishin, Molecular dynamics modeling of self-diffusion along a triple junction, Phys. Rev. B **79**, 174110 (2009).

[108] D. Smirnova, S. Starikov, G. D. Leines, Y. Liang, N. Wang, M. Popov, D. Sangiovanni, I. Abrikosov, R. Drautz, and M. Mrovec, Atomistic description of self-diffusion in molybdenum: A comparative theoretical study of non-arrhenius behavior, Phys. Rev. Mater. **4**, 013605 (2020).

[109] D. Smirnova, S. Starikov, and I. Gordeev, Evaluation of the structure and properties for the high-temperature phase of zirconium from the atomistic simulations, Comput. Mater. Sci. **152**, 51 (2018).

[110] K. Ito and V. Vitek, Atomistic study of non-schmid effects in the plastic yielding of bcc metals, Philos. Mag. A **81**, 1387 (2001).

[111] M. Mrovec, C. Elsaesser, and P. Gumbsch, Interactions between lattice dislocations and twin boundaries in tungsten: A comparative atomistic simulation study, Philos. Mag. **89**, 3179 (2009).

[112] J. Marian, W. Cai, and V. V. Bulatov, Dynamic transitions from smooth to rough to twinning in dislocation motion, Nat. Mater. **3**, 158 (2004).

[113] C. Domain and G. Monnet, Simulation of Screw Dislocation Motion in Iron by Molecular Dynamics Simulations, Phys. Rev. Lett. **95**, 215506 (2005).

[114] L. Ventelon and F. Willaime, Core structure and peierls potential of screw dislocations in α-fe from first principles: Cluster versus dipole approaches, J. Comput.-Aided Mater. Des. **14**, 85 (2007).

[115] C. R. Weinberger, G. J. Tucker, and S. M. Foiles, Peierls potential of screw dislocations in bcc transition metals: Predictions from density functional theory, Phys. Rev. B **87**, 054114 (2013).

[116] L. Dezerald, D. Rodney, E. Clouet, L. Ventelon, and F. Willaime, Plastic anisotropy and dislocation trajectory in bcc metals, Nat. Commun. **7**, 11695 (2016).

[117] L. Ventelon, F. Willaime, E. Clouet, and D. Rodney, *Ab initio* investigation of the peierls potential of screw dislocations in bcc Fe and W, Acta Mater. **61**, 3973 (2013).

[118] T. Suzudo, T. Onitsuka, and K.-i. Fukumoto, Analyzing the cross slip motion of screw dislocations at finite temperatures in body-centered-cubic metals: Molecular statics and dynamics studies, Modell. Simul. Mater. Sci. Eng. **27**, 064001 (2019).

[119] L. Romaner, T. Pradhan, A. Kholtobina, R. Drautz, and M. Mrovec, Theoretical investigation of M111 mixed dislocations in body-centered cubic transition metals (unpublished).

[120] V. Vitek, Intrinsic stacking faults in body-centred cubic crystals, Philos. Mag. **18**, 773 (1968).

[121] J. J. Möller, M. Mrovec, I. Bleskov, J. Neugebauer, T. Hammerschmidt, R. Drautz, C. Elsässer, T. Hickel, and E. Bitzek, {110} planar faults in strained bcc metals: Origins and implications of a commonly observed artifact of classical potentials, Phys. Rev. Mater. **2**, 093606 (2018).

[122] D. Cereceda, A. Stukowski, M. Gilbert, S. Queyreau, L. Ventelon, M.-C. Marinica, J. Perlado, and J. Marian, Assessment of interatomic potentials for atomistic analysis of static and dynamic properties of screw dislocations in w, J. Phys.: Condens. Matter **25**, 085702 (2013).

[123] N. Gunkelmann, I. A. Alhafez, D. Steinberger, H. M. Urbassek, and S. Sandfeld, Nanoscratching of iron: A novel approach to characterize dislocation microstructures, Comput. Mater. Sci. **135**, 181 (2017).

[124] A. Elzas and B. Thijsse, Cohesive law describing crack growth at iron/precipitate interfaces, Comput. Mater. Sci. **134**, 214 (2017).

[125] N. Gao, D. Perez, G. Lu, and Z. Wang, Molecular dynamics study of the interaction between nanoscale interstitial dislocation loops and grain boundaries in bcc iron, J. Nucl. Mater. **498**, 378 (2018).

[126] N. Amadou, T. De Resseguier, A. Dragon, and E. Brambrink, Effects of orientation, lattice defects and temperature on plasticity and phase transition in ramp-compressed single crystal iron, Comput. Mater. Sci. **172**, 109318 (2020).

[127] M. Hummel, C. Böhm, W. Verestek, and S. Schmauder, Introducing a method of constructing realistic closed cell nano-porous iron crystals and MD simulations to investigate the influence of the system size on the stability and the mechanical properties, Comput. Mater. Sci. **166**, 150 (2019).

[128] S. V. Okatov, A. R. Kuznetsov, Y. N. Gornostyrev, V. N. Urtsev, and M. I. Katsnelson, Effect of magnetic state on the γ-α transition in iron: First-principles calculations of the bain transformation path, Phys. Rev. B **79**, 094111 (2009).

[129] C.-S. Lian, J.-T. Wang, and C. Chen, *Ab initio* study of the anharmonic lattice dynamics of iron at the γ-δ phase transition, Phys. Rev. B **92**, 184110 (2015).

[130] I. Bleskov, T. Hickel, J. Neugebauer, and A. Ruban, Impact of local magnetism on stacking fault energies: A first-principles investigation for fcc iron, Phys. Rev. B **93**, 214115 (2016).

[131] I. Seki and K. Nagata, Lattice constant of iron and austenite including its supersaturation phase of carbon, ISIJ Int. **45**, 1789 (2005).

[132] J. Zarestky and C. Stassis, Lattice dynamics of γ-fe, Phys. Rev. B **35**, 4500 (1987).

[133] F. Körmann, T. Hickel, and J. Neugebauer, Influence of magnetic excitations on the phase stability of metals and steels, Curr. Opin. Solid State Mater. Sci. **20**, 77 (2016).

[134] J. R. Morris, C. Z. Wang, K. M. Ho, and C. T. Chan, Melting line of aluminum from simulations of coexisting phases, Phys. Rev. B **49**, 3109 (1994).

[135] A. B. Belonoshko and L. S. Dubrovinsky, Molecular dynamics of NaCl (B1 and B2) and MgO (B1) melting; two-phase simulation, Am. Mineral. **81**, 303 (1996).

[136] S. V. Starikov and V. V. Stegailov, Atomistic simulation of the premelting of iron and aluminum: Implications for high-pressure melting-curve measurements, Phys. Rev. B **80**, 220104(R) (2009).

[137] S. Kim and W. Buyers, Vacancy formation energy in iron by positron annihilation, J. Phys. F: Met. Phys. **8**, L103 (1978).

[138] S. Nikolov, M. A. Wood, A. Cangi, J.-B. Maillet, M.-C. Marinica, A. P. Thompson, M. P. Desjarlais, and J. Tranchida, Quantum-accurate magneto-elastic predictions with classical spin-lattice dynamics, arXiv:2101.07332.

[139] M. Pajda, J. Kudrnovsk, I. Turek, V. Drchal, and P. Bruno, *Ab initio* calculations of exchange interactions, spin-wave stiffness constants, and curie temperatures of Fe, Co, and Ni, Phys. Rev. B **64**, 174402 (2001).

[140] T. L. Gilbert, A phenomenological theory of damping in ferromagnetic materials, IEEE Trans. Magn. **40**, 3443 (2004).

[141] D. C. Wallace, P. Sidles, and G. Danielson, Specific heat of high purity iron by a pulse heating method, J. Appl. Phys. **31**, 168 (1960).

[142] T. Hickel, B. Grabowski, F. Körmann, and J. Neugebauer, Advancing density functional theory to finite temperatures: Methods and applications in steel design, J. Phys.: Condens. Matter **24**, 053202 (2011).

[143] S. Starikov and D. Smirnova, Optimized interatomic potential for atomistic simulation of Zr-Nb alloy, Comput. Mater. Sci. **197**, 110581 (2021).

[144] A. Metsue, A. Oudriss, J. Bouhattate, and X. Feaugas, Contribution of the entropy on the thermodynamic

equilibrium of vacancies in nickel, J. Chem. Phys. **140**, 104705 (2014).

[145] S. S. Naghavi, V. I. Hegde, and C. Wolverton, Diffusion coefficients of transition metals in fcc cobalt, Acta Mater. **132**, 467 (2017).

[146] Y. Gong, B. Grabowski, A. Glensk, F. Körmann, J. Neugebauer, and R. C. Reed, Temperature dependence of the gibbs energy of vacancy formation of fcc ni, Phys. Rev. B **97**, 214106 (2018).

[147] D. Graham and D. Tomlin, Self-diffusion in iron, Philos. Mag. **8**, 1581 (1963).

[148] T. Heumann and R. Imm, Self-diffusion and isotope effect in γ-iron, J. Phys. Chem. Solids **29**, 1613 (1968).

[149] C. Leymonie, *Les Traceurs Radioactifs en Métallurgie Physique* (Dunod, Paris, 1960).

[150] J. Bernardini, P. Gas, E. D. Hondros, and M. Seah, The role of solute segregation in grain boundary diffusion, Proc. R. Soc. London, Ser. A **379**, 159 (1982).

[151] H. Hänsel, L. Stratmann, H. Keller, and H. Grabke, Effects of the grain boundary segregants P, S, C and N on the grain boundary self-diffusivity in α-iron, Acta Metall. **33**, 659 (1985).

[152] S. Divinski, J. Geise, E. Rabkin, and C. Herzig, Grain boundary self-diffusion in α-iron of different purity: Effect of dislocation enhanced diffusion: Dedicated to prof. dr. helmut mehrer on the occasion of his 65th birthday, Z. Metallkd. **95**, 945 (2004).

[153] A. Inoue, H. Nitta, and Y. Iijima, Grain boundary self-diffusion in high purity iron, Acta Mater. **55**, 5910 (2007).

[154] S. Takaki, J. Fuss, H. Kuglers, U. Dedek, and H. Schultz, The resistivity recovery of high purity and carbon doped iron following low temperature electron irradiation, Radiat. Eff. **79**, 87 (1983).

[155] J. Verdone, W. Chambron, and P. Moser, Magnetic anisotropy induced by self-interstitials in low temperature electron irradiated iron, Phys. Status Solidi B **61**, K41 (1974).

[156] Y. Abe, Y. Satoh, and N. Hashimoto, Migration energy of a self-interstitial atom in α-iron estimated by in situ observation of interstitial clusters at low temperatures using high-voltage electron microscopy, Philos. Mag. (2021), doi: 10.1080/14786435.2021.1921873.

[157] R. Johnson, Interstitials and vacancies in α iron, Phys. Rev. **134**, A1329 (1964).

[158] C.-C. Fu, F. Willaime, and P. Ordejón, Stability and Mobility of Mono-and Di-Interstitials in α-Fe, Phys. Rev. Lett. **92**, 175503 (2004).

[159] F. Willaime, C. Fu, M. Marinica, and J. Dalla Torre, Stability and mobility of self-interstitials and small interstitial clusters in α-iron: *Ab initio* and empirical potential calculations, Nucl. Instrum. Methods Phys. Res., Sect. B **228**, 92 (2005).

[160] C. Björkas, K. Nordlund, and M. J. Caturla, Influence of the picosecond defect distribution on damage accumulation in irradiated α-Fe, Phys. Rev. B **85**, 024105 (2012).

[161] S. Bukkuru, U. Bhardwaj, K. S. Rao, A. Rao, M. Warrier, and M. Valsakumar, Kinetics of self-interstitial migration in bcc and fcc transition metals, Mater. Res. Express **5**, 035513 (2018).

[162] D. A. Terentyev, L. Malerba, and M. Hou, Dimensionality of interstitial cluster motion in bcc-Fe, Phys. Rev. B **75**, 104108 (2007).

[163] S. Starikov, D. Smirnova, M. Mrovec, and R. Drautz, Development of new interatomic potential for atomistic simulation of defects behaviour in Fe-Cr-H ternary system, Nucl. Mater. Conf. (2020), doi: 10.13140/RG.2.2.14024.96000/1.